Measurement of Charm and Beauty Jets in Deep Inelastic Scattering at HERA

H1 Collaboration

Abstract

Measurements of cross sections for events with charm and beauty jets in deep inelastic scattering at HERA are presented. Events with jets of transverse energy $E_T^{\text{jet}} > 6$ GeV and pseudorapidity $-1.0 < \eta^{\text{jet}} < 1.5$ in the laboratory frame are selected in the kinematic region of photon virtuality $Q^2 > 6$ GeV^2 and inelasticity variable $0.07 < y < 0.625$. Measurements are also made requiring a jet in the Breit frame with $E_T^{*\text{jet}} > 6$ GeV. The data were collected with the H1 detector in the years 2006 and 2007 corresponding to an integrated luminosity of 189 pb^{-1}. The numbers of charm and beauty jets are determined using variables reconstructed using the H1 vertex detector with which the impact parameters of the tracks to the primary vertex and the position of secondary vertices are measured. The measurements are compared with QCD predictions and with previous measurements where heavy flavours are identified using muons.

F.D. Aaron[5,49], C. Alexa[5], V. Andreev[25], S. Backovic[30], A. Baghdasaryan[38], E. Barrelet[29],
W. Bartel[11], K. Begzsuren[35], A. Belousov[25], J.C. Bizot[27], V. Boudry[28], I. Bozovic-Jelisavcic[2],
J. Bracinik[3], G. Brandt[11], M. Brinkmann[11], V. Brisson[27], D. Britzger[11], D. Bruncko[16],
A. Bunyatyan[13,38], G. Buschhorn[26,†], L. Bystritskaya[24], A.J. Campbell[11], K.B. Cantun Avila[22],
F. Ceccopieri[4], K. Cerny[32], V. Cerny[16,47], V. Chekelian[26], A. Cholewa[11], J.G. Contreras[22],
J.A. Coughlan[6], J. Cvach[31], J.B. Dainton[18], K. Daum[37,43], M. Deák[11], B. Delcourt[27],
J. Delvax[4], E.A. De Wolf[4], C. Diaconu[21], M. Dobre[12,51,52], V. Dodonov[13], A. Dossanov[26],
A. Dubak[30,46], G. Eckerlin[11], V. Efremenko[24], S. Egli[36], A. Eliseev[25], E. Elsen[11], L. Favart[4],
A. Fedotov[24], R. Felst[11], J. Feltesse[10,48], J. Ferencei[16], D.-J. Fischer[11], M. Fleischer[11],
A. Fomenko[25], E. Gabathuler[18], J. Gayler[11], S. Ghazaryan[11], A. Glazov[11], L. Goerlich[7],
N. Gogitidze[25], M. Gouzevitch[11], C. Grab[40], A. Grebenyuk[11], T. Greenshaw[18], B.R. Grell[11],
G. Grindhammer[26], S. Habib[11], D. Haidt[11], C. Helebrant[11], R.C.W. Henderson[17],
E. Hennekemper[15], H. Henschel[39], M. Herbst[15], G. Herrera[23], M. Hildebrandt[36], K.H. Hiller[39],
D. Hoffmann[21], R. Horisberger[36], T. Hreus[4,44], F. Huber[14], M. Jacquet[27], X. Janssen[4],
L. Jönsson[20], A.W. Jung[15], H. Jung[11,4], M. Kapichine[9], J. Katzy[11], I.R. Kenyon[3],
C. Kiesling[26], M. Klein[18], C. Kleinwort[11], T. Kluge[18], A. Knutsson[11], R. Kogler[26], P. Kostka[39],
M. Kraemer[11], J. Kretzschmar[18], A. Kropivnitskaya[24], K. Krüger[15], K. Kutak[11],
M.P.J. Landon[19], W. Lange[39], G. Laštovička-Medin[30], P. Laycock[18], A. Lebedev[25],
V. Lendermann[15], S. Levonian[11], K. Lipka[11,51], B. List[12], J. List[11], N. Loktionova[25],
R. Lopez-Fernandez[23], V. Lubimov[24], A. Makankine[9], E. Malinovski[25], P. Marage[4],
H.-U. Martyn[1], S.J. Maxfield[18], A. Mehta[18], A.B. Meyer[11], H. Meyer[37], J. Meyer[11],
S. Mikocki[7], I. Milcewicz-Mika[7], F. Moreau[28], A. Morozov[9], J.V. Morris[6], M.U. Mozer[4],
M. Mudrinic[2], K. Müller[41], Th. Naumann[39], P.R. Newman[3], C. Niebuhr[11], A. Nikiforov[11],
D. Nikitin[9], G. Nowak[7], K. Nowak[11], J.E. Olsson[11], S. Osman[20], D. Ozerov[24], P. Pahl[11],
V. Palichik[9], I. Panagoulias[l,11,42], M. Pandurovic[2], Th. Papadopoulou[l,11,42], C. Pascaud[27],
G.D. Patel[18], E. Perez[10,45], A. Petrukhin[11], I. Picuric[30], S. Piec[11], H. Pirumov[14], D. Pitzl[11],
R. Plačakytė[11], B. Pokorny[32], R. Polifka[32], B. Povh[13], V. Radescu[14], A.J. Rahmat[18],
N. Raicevic[30], T. Ravdandorj[35], P. Reimer[31], E. Rizvi[19], P. Robmann[41], R. Roosen[4],
A. Rostovtsev[24], M. Rotaru[5], J.E. Ruiz Tabasco[22], S. Rusakov[25], D. Šálek[32], D.P.C. Sankey[6],
M. Sauter[14], E. Sauvan[21], S. Schmitt[11], L. Schoeffel[10], A. Schöning[14],
H.-C. Schultz-Coulon[15], F. Sefkow[11], L.N. Shtarkov[25], S. Shushkevich[26], T. Sloan[17],
I. Smiljanic[2], Y. Soloviev[25], P. Sopicki[7], D. South[8], V. Spaskov[9], A. Specka[28], Z. Staykova[11],
M. Steder[11], B. Stella[33], G. Stoicea[5], U. Straumann[41], D. Sunar[4], T. Sykora[4], G. Thompson[19],
P.D. Thompson[3], T. Toll[11], T.H. Tran[27], D. Traynor[19], P. Truöl[41], I. Tsakov[34],
B. Tseepeldorj[35,50], J. Turnau[7], K. Urban[15], A. Valkárová[32], C. Vallée[21], P. Van Mechelen[4],
A. Vargas Trevino[11], Y. Vazdik[25], M. von den Driesch[11], D. Wegener[8], E. Wünsch[11],
J. Žáček[32], J. Zálešák[31], Z. Zhang[27], A. Zhokin[24], H. Zohrabyan[38], and F. Zomer[27]

[1] *I. Physikalisches Institut der RWTH, Aachen, Germany*
[2] *Vinca Institute of Nuclear Sciences, Belgrade, Serbia*
[3] *School of Physics and Astronomy, University of Birmingham, Birmingham, UK[b]*
[4] *Inter-University Institute for High Energies ULB-VUB, Brussels and Universiteit Antwerpen, Antwerpen, Belgium[c]*
[5] *National Institute for Physics and Nuclear Engineering (NIPNE) , Bucharest, Romania[m]*
[6] *Rutherford Appleton Laboratory, Chilton, Didcot, UK[b]*
[7] *Institute for Nuclear Physics, Cracow, Poland[d]*

1

[8] *Institut für Physik, TU Dortmund, Dortmund, Germany[a]*

[9] *Joint Institute for Nuclear Research, Dubna, Russia*

[10] *CEA, DSM/Irfu, CE-Saclay, Gif-sur-Yvette, France*

[11] *DESY, Hamburg, Germany*

[12] *Institut für Experimentalphysik, Universität Hamburg, Hamburg, Germany[a]*

[13] *Max-Planck-Institut für Kernphysik, Heidelberg, Germany*

[14] *Physikalisches Institut, Universität Heidelberg, Heidelberg, Germany[a]*

[15] *Kirchhoff-Institut für Physik, Universität Heidelberg, Heidelberg, Germany[a]*

[16] *Institute of Experimental Physics, Slovak Academy of Sciences, Košice, Slovak Republic[f]*

[17] *Department of Physics, University of Lancaster, Lancaster, UK[b]*

[18] *Department of Physics, University of Liverpool, Liverpool, UK[b]*

[19] *Queen Mary and Westfield College, London, UK[b]*

[20] *Physics Department, University of Lund, Lund, Sweden[g]*

[21] *CPPM, Aix-Marseille Université, CNRS/IN2P3, Marseille, France*

[22] *Departamento de Fisica Aplicada, CINVESTAV, Mérida, Yucatán, México[j]*

[23] *Departamento de Fisica, CINVESTAV IPN, México City, México[j]*

[24] *Institute for Theoretical and Experimental Physics, Moscow, Russia[k]*

[25] *Lebedev Physical Institute, Moscow, Russia[e]*

[26] *Max-Planck-Institut für Physik, München, Germany*

[27] *LAL, Université Paris-Sud, CNRS/IN2P3, Orsay, France*

[28] *LLR, Ecole Polytechnique, CNRS/IN2P3, Palaiseau, France*

[29] *LPNHE, Université Pierre et Marie Curie Paris 6, Université Denis Diderot Paris 7, CNRS/IN2P3, Paris, France*

[30] *Faculty of Science, University of Montenegro, Podgorica, Montenegro[e]*

[31] *Institute of Physics, Academy of Sciences of the Czech Republic, Praha, Czech Republic[h]*

[32] *Faculty of Mathematics and Physics, Charles University, Praha, Czech Republic[h]*

[33] *Dipartimento di Fisica Università di Roma Tre and INFN Roma 3, Roma, Italy*

[34] *Institute for Nuclear Research and Nuclear Energy, Sofia, Bulgaria[e]*

[35] *Institute of Physics and Technology of the Mongolian Academy of Sciences, Ulaanbaatar, Mongolia*

[36] *Paul Scherrer Institut, Villigen, Switzerland*

[37] *Fachbereich C, Universität Wuppertal, Wuppertal, Germany*

[38] *Yerevan Physics Institute, Yerevan, Armenia*

[39] *DESY, Zeuthen, Germany*

[40] *Institut für Teilchenphysik, ETH, Zürich, Switzerland[i]*

[41] *Physik-Institut der Universität Zürich, Zürich, Switzerland[i]*

[42] *Also at Physics Department, National Technical University, Zografou Campus, GR-15773 Athens, Greece*

[43] *Also at Rechenzentrum, Universität Wuppertal, Wuppertal, Germany*

[44] *Also at University of P.J. Šafárik, Košice, Slovak Republic*

[45] *Also at CERN, Geneva, Switzerland*

[46] *Also at Max-Planck-Institut für Physik, München, Germany*

[47] *Also at Comenius University, Bratislava, Slovak Republic*

[48] *Also at DESY and University Hamburg, Helmholtz Humboldt Research Award*

[49] *Also at Faculty of Physics, University of Bucharest, Bucharest, Romania*

1   Introduction

The production of heavy flavour quarks in deep inelastic scattering (DIS) at the HERA electron–proton collider is of particular interest for testing calculations in the framework of perturbative quantum chromodynamics (QCD). The process has the special feature of involving two hard scales: the square root of the photon virtuality Q and the heavy quark mass m. In the case of heavy flavour jet production the transverse energy E_T of the jet provides a further hard scale. Therefore, the measurement of jets with large E_T provides additional information in the region where the heavy quarks have high transverse momentum and the theoretical uncertainties are reduced. In leading order (LO) QCD, the photon-gluon fusion (PGF) processes $ep \rightarrow ec\bar{c}X$ and $ep \rightarrow eb\bar{b}X$ are the dominant production mechanisms for charm (c) and beauty (b) quarks respectively.

The inclusive c and b quark cross sections and the derived structure functions have been measured in DIS at HERA using the 'inclusive lifetime' technique [1, 2] and found to be well described by next to leading order (NLO) QCD. Measurements of the charm cross section using the technique of D meson tagging have also been made [3, 4] and are found to be in good agreement with those using inclusive lifetime information. Measurements of the total charm and beauty cross sections have been made by identifying their decays to muons [5]. In the charm case these measurements show good agreement with the data extracted using the inclusive lifetime technique, but are somewhat larger in the case of beauty.

Measurements of beauty quark production using muon tagging have also been made for DIS events containing a high E_T jet in either the Breit frame [6, 7] or in the laboratory frame [8]. As in the muon inclusive case [5] the results were found to be somewhat higher than NLO QCD predictions, in particular at low values of Q^2. In photoproduction, measurements of beauty have been made using various lepton tagging techniques and have been found to be either somewhat higher than [9] or in agreement with [10] NLO QCD. A measurement in the Breit frame of the production of D^* mesons in association with high E_T dijets [11] was found to be in agreement with NLO QCD predictions within the statistics of the measurement. A measurement of c and b jets in photoproduction has been made [12], which uses a similar method to distinguish heavy flavour jets as in the present analysis. The results were found to be in good agreement with NLO QCD.

This paper reports on measurements of the cross sections for events with a c or b jet in DIS at HERA. The analysis uses an inclusive lifetime technique following a similar procedure as used in [1] to distinguish the jets that contain c or b flavoured hadrons from those containing light flavoured hadrons only. The data are analysed in the laboratory frame of reference to match the acceptance of the H1 detector and a heavy flavour jet with the highest transverse energy $E_T^{\mathrm{jet}} > 6 \,\mathrm{GeV}$ is required. The measurements in the laboratory frame are compared with b quark production measurements obtained from muon tagging [8]. The analysis is extended to the Breit frame of reference requiring a jet with transverse energy of $E_T^{*\mathrm{jet}} > 6 \,\mathrm{GeV}$. The results are also compared with b quark measurements obtained from muon tagging [7]. The cross section measurements in both frames of reference are compared with an NLO QCD program [13].

The data for this analysis were recorded in the years 2006 and 2007 with integrated luminosities of $135 \,\mathrm{pb}^{-1}$ taken in e^+p mode and $54 \,\mathrm{pb}^{-1}$ taken in e^-p mode . The ep centre of mass energy is $\sqrt{s} = 319 \,\mathrm{GeV}$, with a proton beam energy of $920 \,\mathrm{GeV}$ and electron[1] beam

---

[1]In this paper the term 'electron' also denotes 'positron' unless explicitly stated.

energy of 27.6 GeV. The measurements are made for the kinematic region of photon virtuality $Q^2 > 6$ GeV^2 and inelasticity variable $0.07 < y < 0.625$.

Jets containing heavy flavoured hadrons are distinguished from those containing only light flavours using variables reconstructed using the H1 vertex detector. The most important of these inputs are the transverse displacement of tracks from the primary vertex and the reconstructed position of a secondary vertex in the transverse plane. Hadrons from heavy quark decays typically have longer lifetimes than light hadrons and thus produce tracks that have a significant displacement from the primary vertex. For jets with three or more tracks in the vertex detector the reconstructed variables are used as input to a neural network to discriminate beauty from charm jets.

2   Monte Carlo Simulation

Monte Carlo simulations are used to correct for the effects of the finite detector resolution, acceptance and efficiency. The Monte Carlo program RAPGAP [14] is used to generate DIS events for the processes $ep \rightarrow eb\bar{b}X$, $ep \rightarrow ec\bar{c}X$ and $ep \rightarrow eqX$ where q is a light quark of flavour u, d or s. RAPGAP combines $\mathcal{O}(\alpha_s)$ matrix elements with higher order QCD effects modelled by parton showers. The heavy flavour event samples are generated according to the massive photon gluon fusion (PGF) matrix element [15] with the mass of the c and b quarks set to $m_c = 1.5$ GeV and $m_b = 4.75$ GeV, respectively. The DIS cross section is calculated using the leading order 3-flavour parton density function (PDF) set MRST2004F3LO [16].

The partonic system for the generated events is fragmented according to the Lund string model [17] implemented within the PYTHIA program [18]. The c and b quarks are hadronised according to the Bowler fragmentation function [19] using the parameters $a = 0.4$ GeV^{-2}, $b = 1.03$ GeV^{-2} and $r_Q = 1$ [20]. The HERACLES program [21] calculates single photon radiative emissions off the lepton line, virtual and electroweak corrections.

PYTHIA is used to simulate the background contribution from photoproduction $\gamma p \rightarrow X$. The assumed heavy flavour cross sections are in agreement with the measurements made by H1 [12].

The samples of events generated for the uds, c, and b processes are passed through a detailed simulation of the detector response based on the GEANT3 program [22], and through the same reconstruction software as is used for the data.

3   QCD Models

The jet cross section data in this paper are compared with two approaches within QCD:

Firstly, the data are compared with the predictions of Monte Carlo programs based on leading order matrix elements with the effect of higher orders modelled by initial and final state parton showers. The predictions from the RAPGAP Monte Carlo program are calculated with the same settings as described in section 2. The renormalisation and factorisation scales are set

5

to $\mu_r = \mu_f = Q$. The Monte Carlo program CASCADE [23] is also used to produce predictions for the b and c jet cross sections. CASCADE is based on the CCFM [24] evolution equation and uses off shell matrix elements convoluted with k_T unintegrated proton parton distributions. The CASCADE predictions use the A0 PDF set with $m_c = 1.5$ GeV and $m_b = 4.75$ GeV, and $\mu_r = \sqrt{Q^2 + p_T^2 + 4m^2}$, where p_T is the transverse momentum of the heavy quark in the virtual photon-proton centre of mass frame. Due to the fact that the predictions are based on leading order matrix elements the uncertainty on the normalisation of the cross sections is large, and is not quantified here.

Secondly, the data are compared with the predictions of the NLO QCD program HVQDIS [13]. The program is based on the fixed flavour numbering scheme (FFNS) which uses the massive PGF $\mathcal{O}(\alpha_s^2)$ matrix element [25] and provides weighted events with two or three outgoing partons, i.e. a heavy quark pair and possibly an additional light parton. The calculations are made using the same settings for the choice of the quark masses as for the Monte Carlo programs above: $m_c = 1.5$ GeV, $m_b = 4.75$ GeV. At NLO the predictions of QCD depend on the choice of the scales μ_r and μ_f. To investigate the dependence of the predictions on the scales two example choices are made. Firstly, the scale $\mu_r = \mu_f = \sqrt{(Q^2 + p_T^2 + m^2)/2}$, where p_T is the transverse momentum of the heavy quark with the highest value of p_T in the virtual photon-parton centre of mass frame, is used. This choice of scale is motivated by the comparison of NLO QCD with recent measurements of inclusive jet data by H1 [26]. Secondly, the scale $\mu_r = \mu_f = \sqrt{Q^2 + 4m^2}$ is selected. This scale has been used in the comparison of HVQDIS with H1 inclusive and dijet D^* DIS data [4,11]. Parton level jet cross sections are calculated by applying the jet algorithm (see section 5.2) to the outgoing partons from HVQDIS in either the laboratory or Breit frames of reference. Since HVQDIS provides cross sections at the parton level, corrections to the hadron level are needed in order to compare to the data. These corrections are calculated using the RAPGAP Monte Carlo event generator. In each kinematic bin of the measurement, the ratio C_{had} of the RAPGAP hadron level to parton level cross sections is calculated and applied as a correction factor to the NLO calculation. The hadron level corrections generally amount to a change in the prediction by $\leq 6\%$ for charm and $\leq 15\%$ for beauty.

In QCD fits to global hard-scattering data the parton density functions are usually extracted using the general mass variable flavour number scheme (GM VFNS) [27–33] for heavy quarks. This scheme, which interpolates from the massive approach at low scale values to a 'massless' approach at high scale values, provides a theoretically accurate description of heavy flavour production. Recently, a set of PDFs [34] compatible with the FFNS were generated, using the standard GM VFNS PDFs [35] to facilitate comparison of the heavy flavour final state data with up-to-date PDFs.

Predictions are made using three different sets of PDFs: the MSTW08FF3 [34] set extracted using the GM VFNS but evolved using the FFNS in order to be compatible with HVQDIS; the CTEQ5F3 [36] set extracted using the FFNS; and with the CTEQ6.6 [29] set extracted using the GM VFNS. The CTEQ6.6 PDF set uses a variable flavour definition of the running coupling α_s which is different to the fixed flavour definition assumed in HVQDIS. However, the inaccuracy introduced by this incompatibility is likely to be compensated by using an up-to-date PDF set [37].

As an estimate of the uncertainty on each of the NLO QCD predictions the scales μ_r and μ_f are varied simultaneously by factors of 0.5 and 2, m_c is changed by ± 0.2 GeV and m_b is

6

changed by ± 0.25 GeV. The uncertainty on C_{had} is estimated by replacing, in the RAPGAP simulation, the Bowler [19] fragmentation function by the symmetric function in the Lund model [38], corresponding to $r_Q = 0$.

4 H1 Detector

Only a short description of the H1 detector is given here; a more complete description may be found elsewhere [39, 40]. A right-handed coordinate system is employed at H1, with its origin at the nominal interaction vertex, that has its Z-axis pointing in the proton beam, or forward, direction and X (Y) pointing in the horizontal (vertical) direction. The pseudorapidity is related to the polar angle θ by $\eta = -\ln\tan(\theta/2)$.

Charged particles are measured in the central tracking detector (CTD). This device consists of two cylindrical drift chambers interspersed with orthogonal chambers to improve the Z-coordinate reconstruction and multi-wire proportional chambers mainly used for triggering. The CTD is operated in a uniform solenoidal 1.16 T magnetic field, enabling the momentum measurement of charged particles over the polar angular range[2] $20° < \theta < 160°$.

The CTD tracks are linked to hits in the vertex detector, the central silicon tracker (CST) [41], to provide precise spatial track reconstruction. The CST consists of two layers of double-sided silicon strip detectors surrounding the beam pipe, covering an angular range of $30° < \theta < 150°$ for tracks passing through both layers. The information on the Z-coordinate of the CST tracks is not used in the analysis presented in this paper. For CTD tracks with CST hits in both layers the transverse distance of closest approach (DCA) to the nominal vertex in X–Y, averaged over the azimuthal angle, is measured to have a resolution of $43\ \mu\text{m} \oplus 51\ \mu\text{m}/(P_T[\text{GeV}])$, where the first term represents the intrinsic resolution (including alignment uncertainty) and the second term is the contribution from multiple scattering in the beam pipe and the CST; P_T is the transverse momentum of the particle. The efficiency for linking hits in both layers of the CST to a CTD track is around 84%. The efficiency for finding tracks in the CTD is greater than 95%.

The track detectors are surrounded in the forward and central directions ($4° < \theta < 155°$) by a finely grained liquid argon calorimeter (LAr) and in the backward region ($153° < \theta < 178°$) by a lead-scintillating fibre calorimeter (SPACAL) with electromagnetic and hadronic sections. These calorimeters provide energy and angular reconstruction for final state particles from the hadronic system and are also used in this analysis to measure and identify the scattered electron.

Electromagnetic calorimeters situated downstream in the electron beam direction allow detection of photons and electrons scattered at very low Q^2. The luminosity is measured with these calorimeters from the rate of photons produced in the Bethe-Heitler process $ep \rightarrow ep\gamma$.

---

[2]The angular coverage of each detector component is given for the interaction vertex in its nominal position i.e. the position of the centre of the detector.

5 Experimental Method

5.1 DIS Event Selection

The events are triggered by a compact, isolated electromagnetic cluster in either the LAr or SPACAL calorimeters in combination with a loose track requirement such that the overall trigger efficiency is almost 100%. The electromagnetic cluster with the highest transverse energy, which also passes stricter offline criteria is taken as the scattered electron. The Z-position of the interaction vertex, reconstructed by one or more charged tracks in the tracking detectors, must be within $\pm 20 \, \mathrm{cm}$ of the centre of the detector to match the acceptance of the CST.

Photoproduction events and DIS events with a hard photon radiated from the initial state electron are suppressed by requiring $\sum_i (E_i - p_{Z,i}) > 35 \, \mathrm{GeV}$. Here, E_i and $p_{Z,i}$ denote the energy and longitudinal momentum components of a particle and the sum is over all final state particles including the scattered electron and the hadronic final state (HFS). The HFS particles are reconstructed using a combination of tracks and calorimeter deposits in an energy flow algorithm that avoids double counting [42].

The event kinematics, Q^2 and y, are reconstructed with the '$e\Sigma$' method [43], which uses the scattered electron and the HFS. In order to have good acceptance for the scattered electron in the calorimeters the events are selected in the range $Q^2 > 6 \, \mathrm{GeV}^2$. The analysis is restricted to $0.07 < y < 0.625$ in order to ensure there is a high probability of at least one jet within the acceptance of the CST and to reduce the photoproduction background. The position of the beam interaction region in X and Y (beam spot) is derived from tracks with CST hits and updated regularly to account for drifts during beam storage.

5.2 Jet Reconstruction

Jets are reconstructed using the inclusive longitudinally invariant k_T algorithm with the massless P_T recombination scheme and the distance parameter $R_0 = 1$ in the $\eta - \phi$ plane [44]. The algorithm is first run in the laboratory frame using all reconstructed HFS particles and the resultant jets are required to have transverse energy $E_T^{\mathrm{jet}} > 1.5 \, \mathrm{GeV}$, in the angular range $-1.0 < \eta^{\mathrm{jet}} < 1.5$. The η range is asymmetric since the y range chosen means few jets have $\eta < -1.0$. This cut also means that the jets are not near the boundary between the LAr and SPACAL calorimeters. Jets are reconstructed from the Monte Carlo simulation using an identical procedure to that of the data.

The Monte Carlo simulation is also used to define hadron and parton level jets before they are processed by the simulation of the detector response. Hadron level jets are defined by running the same jet algorithm as for reconstructed jets using all final state particles, including neutrinos, but excluding the scattered electron. A Monte Carlo jet at the reconstructed or hadron level is defined as a 'b jet' if there is at least one b hadron within a cone of radius 1 about the jet axis in the $\eta - \phi$ plane. A jet is defined as a 'c jet' if there is at least one c hadron within the same cone and that c hadron does not arise from the decay of a b hadron. Jets that have not been classified as c or b jets are called 'light jets'. Parton level jets are defined for the Monte Carlo

8

samples and for the NLO calculation by running the same jet algorithm on final state partons. A parton level jet is defined as a b jet if there is at least one b quark within a cone of radius 1 about the jet axis in the $\eta - \phi$ plane. A parton level jet is defined as a c jet if there is at least one c quark and no b quark within the cone.

In order to compare with perturbative calculations a good correlation between the parton level and hadron level jets is necessary. A jet with high transverse energy is required in either the laboratory frame of reference $E_T^{\mathrm{jet}} > 6$ GeV or in the Breit frame $E_T^{*\mathrm{jet}} > 6$ GeV. For the analysis in the laboratory frame the cross section is measured as a function of E_T^{jet}, η^{jet}, Q^2, the number of jets N_{jet} with $E_T^{\mathrm{jet}} > 6$ GeV and also for the integrated sample. For the analysis in the Breit frame the flavour of the jet is defined in the laboratory, as described above, for jets in the range $E_T^{\mathrm{jet}} > 1.5$ GeV and $-1.0 < \eta^{\mathrm{jet}} < 1.5$. For events satisfying this condition all the final state particles are then boosted to the Breit frame using the four vector of the scattered electron and the value of Bjorken x obtained from $x = Q^2/sy$. The jet finding algorithm is rerun on the boosted particles. The jets in the Breit frame are required to have a transverse energy $E_T^{*\mathrm{jet}} > 6$ GeV and to have a pseudorapidity, when boosted back to the laboratory frame, in the range $-1.0 < \eta^{\mathrm{jet}} < 1.5$. The cross section is measured as a function of $E_T^{*\mathrm{jet}}$ and Q^2 for the selected events. The data, measured as a function of Q^2, in both reference frames are compared with b jet data obtained from muon tagging, after correcting those results for the muon phase space and other, smaller, differences between the kinematic ranges of the measurements.

5.3   Jet Flavour Separation

In the analysis presented in this paper the flavour of the event is defined as the flavour of the jet with the highest E_T^{jet} in the laboratory. Therefore, the measured cross sections are proportional to the number of events with a jet rather than the number of jets in an event.

The separation of b, c and light jets is only briefly described here. The procedure closely follows that described in [1]. The separation is performed using the properties of those tracks which are within a cone of radius 1 from the jet axis in the $\eta - \phi$ plane. The tracks are reconstructed in the CTD and must have at least 2 CST hits and have transverse momentum greater than 0.3 GeV. The impact parameter δ of a track is the transverse DCA of the track to the beam spot point. Tracks with $\delta > 0.1$ cm are rejected to suppress contributions from the decays of long-lived strange particles.

The number of tracks in the jet after these selections is called N_{track}. The track significance S is defined as $S = \delta/\sigma(\delta)$, where $\sigma(\delta)$ is the uncertainty on δ. If the angle α between the azimuthal angle of the jet ϕ_{jet} and the line joining the primary vertex to the point of DCA is less than $90°$, the significance is defined as positive [1]. It is defined as negative otherwise. The significances S_1, S_2 and S_3 are defined as the significance of the track with the highest, second highest and third highest absolute significance, respectively. The selected tracks are also used to reconstruct the position of the secondary vertex.

The jets are separated into three independent samples. For each sample a different distribution is used to separate the light, b and c jets. The S_1 distribution is used for jets where $N_{\mathrm{track}} = 1$ or S_1 and S_2 have opposite signs. The S_2 distribution is used for the remaining jets

with $N_{\text{track}} = 2$ or where S_3 has a different sign to S_1 and S_2. Generally S_2 has a better discrimination between light and heavy flavour jets than S_1, since the chance of reconstructing 2 high significance tracks is small for jets where all the tracks arise at the primary vertex. For jets with $N_{\text{track}} \geq 3$ where S_1, S_2 and S_3 all have the same sign an artificial neural network (NN) is used to produce a distribution that combines several variables in order to provide an optimal discrimination between b and c jets. The inputs to the NN are S_1, S_2, S_3, the significance of the transverse distance between the secondary and primary vertex, the transverse momenta of the tracks with the highest and second highest transverse momentum, N_{track}, and the number of reconstructed tracks at the secondary vertex. The NN is trained using a sample of inclusive heavy flavour DIS Monte Carlo events, with b events as 'signal' and c events as 'background', as described in [1]. The NN output is signed according to the sign of S_1.

The three distributions that are used in the flavour separation are shown in figure 1. It can be seen that the distributions are asymmetric, mainly due to the tracks arising from heavy flavour decays. The NN output gives absolute values in the range from about 0.2 to 0.95. The light jet distribution is approximately symmetric and peaks towards low absolute values; the c and b distributions are asymmetric with more positive than negative entries; the b events are peaked towards 1, whereas the c events are peaked towards 0. For the S_1, S_2 and NN output distributions the data are well described by the Monte Carlo simulation and the contribution from photoproduction is very small.

Since the S_1, S_2 and NN output distributions for light jets are nearly symmetric around zero the sensitivity to the modelling of the light jets can be reduced by subtracting the contents of the negative bins from the contents of the corresponding positive bins. The subtracted distributions are shown in figure 2. The resulting distributions are dominated by c jets, with a b jet fraction increasing towards the upper end of the distributions. Overall the light jets contribute only a small fraction.

The fractions of events with c, b and light jets in the data are extracted using a least squares simultaneous fit to the subtracted S_1, S_2 and NN output distributions (as in figure 2) and the total number of events after DIS and jet selection. Only those bins in the significance distributions which have at least 25 events before subtraction are considered in the fit, since Gaussian errors are assumed. The last fitted bin of the significance distributions, which usually has the lowest statistics, is made 3 times as wide as the other bins (see figure 2).

The uds (light), c and b RAPGAP Monte Carlo simulation samples are used as templates. The templates are scaled by factors ρ_l, ρ_c and ρ_b, respectively, to give the best fit. The Monte Carlo samples are weighted to the equivalent luminosity of the data sample so that the ρ scale factors are the ratio between the cross sections of the Monte Carlo models and the data. The PYTHIA Monte Carlo program is used to estimate photoproduction background and found to be 0.8% overall. The contributions of light, c and b jets in photoproduction are fixed to the PYTHIA prediction. Only the statistical errors of the data and Monte Carlo simulations are considered in the fit.

The fitted ρ parameters for the whole kinematic range and for each of the differential distributions are listed in table 1. The table includes the correlation coefficients of the fit parameters. The fitted parameter ρ_c is seen to be anti-correlated with both ρ_l and ρ_b, due to c jets being a significant contribution to the total jet cross section. The magnitude of the correlation C_{lc} is

greater than C_{bc} reflecting the fact that the shapes of the Monte Carlo templates for c jets are more similar to those for the light jets than those for b jets. Also included in the table is the $\chi^2/\text{n.d.f.}$ for each fit evaluated using statistical errors only. Acceptable values are obtained for all fits.

The fitted ρ_c value for each bin is converted to a c jet cross section using

$$\sigma_c = \frac{\rho_c N_c^{\text{MCgen}}}{\mathcal{L} C_{\text{rad}}}, \tag{1}$$

where N_c^{MCgen} is the number of generated events that pass the DIS kinematic selection of the bin and which contain a c jet passing the jet cuts of the bin at the hadron level, $\mathcal{L}$ is the integrated luminosity of 189 pb^{-1} and C_{rad} is a radiative correction, calculated from the HERACLES Monte Carlo program. The number of generated events N_c^{MCgen} is calculated after normalising the luminosity of the Monte Carlo samples to that of the data as described above. The b cross sections are evaluated in a corresponding manner. The differential cross sections are obtained from the cross sections integrated over the bin interval by dividing by the size of the bin interval, and no further bin centre correction is applied.

6   Systematic Uncertainties

The following uncertainties are taken into account in order to evaluate the systematic error.

- The uncertainty in the δ resolution of the tracks is estimated by varying the resolution by an amount that encompasses any difference between the data and the simulation. This was achieved by applying an additional Gaussian smearing in the Monte Carlo simulation of 200 μm to 5% of randomly selected tracks and 12 μm to the rest.

- The uncertainty due to the track efficiency uncertainty is estimated by varying the efficiency of the CTD by $\pm 1\%$ and that of the CST by $\pm 2\%$.

- The uncertainties on the various D and B meson lifetimes, decay branching fractions and mean charge multiplicities are estimated by varying the input values of the Monte Carlo simulation by the errors on the world average measurements. For the branching fractions of b quarks to hadrons and the lifetimes of the D and B mesons the central values and errors on the world averages are taken from [45]. For the branching fractions of c quarks to hadrons the values and uncertainties are taken from the e^+e^- average of [46], which are consistent with measurements made in DIS at HERA [47]. For the mean charged track multiplicities the values and uncertainties for c and b quarks are taken from MarkIII [48] and LEP/SLD [49] measurements, respectively.

- The uncertainty on the fragmentation function of the heavy quarks is estimated by reweighting the events according to the longitudinal string momentum fraction z carried by the heavy hadron in the Lund model using weights of $(1 \mp 0.7) \cdot (1 - z) + z \cdot (1 \pm 0.7)$ for charm quarks and by $(1 \mp 0.5) \cdot (1 - z) + z \cdot (1 \pm 0.5)$ for beauty quarks. The variations for the charm fragmentation are motivated by encompassing the differences between the Monte Carlo simulation and H1 D^* data [50]. The size of the variations is reduced for beauty compared with charm since the fragmentation spectrum is harder.

- The uncertainty on the QCD model of heavy quark production is estimated by reweighting the jet transverse momentum and pseudorapidity by $(E_T^{\mathrm{jet}}/(10 \text{ GeV}))^{\pm 0.2}$ and $(1 \pm \eta^{\mathrm{jet}})^{\pm 0.15}$ for charm jets and $(E_T^{\mathrm{jet}}/(10 \text{ GeV}))^{\pm 0.3}$ and $(1 \pm \eta^{\mathrm{jet}})^{\pm 0.3}$ for beauty jets. These values are obtained by comparing these variations with the measured cross sections.

- The uncertainty on the asymmetry of the light jet δ distribution is estimated by repeating the fits with the subtracted light jet distributions (figure 2) changed by $\pm 30\%$. The light jet asymmetry was checked to be within this uncertainty by comparing the asymmetry of Monte Carlo simulation events to that of the data for K^0 candidates, in the region $0.1 < |\delta| < 0.5$ cm, where the light jet asymmetry is enhanced.

- The uncertainty on the reconstruction of ϕ_{jet} is estimated by shifting its value by $\pm 2°$. The uncertainty was evaluated by comparing the distribution of the difference between ϕ_{jet} and the track azimuthal angle in data and Monte Carlo simulation.

- The uncertainty arising from the hadronic energy scale is estimated by changing the hadronic energy by $\pm 2\%$ for jets in the laboratory and $\pm 4\%$ for the jets in the Breit frame.

- The uncertainty arising from the electron energy scale and polar angle is estimated by changing the electron energy by $\pm 1\%$ and the polar angle by ± 1 mrad.

- The uncertainty in the photoproduction background is estimated by varying the expected number of events by $\pm 100\%$.

- The uncertainty on the luminosity is 4%.

- The uncertainty on the radiative correction is 2%.

The above systematic uncertainties are evaluated by making the changes described above to the Monte Carlo simulation and repeating the procedure to evaluate the c and b cross sections, including the fits. The uncertainties are evaluated separately for each measurement bin and are treated as correlated except for the radiative corrections.

The most important sources of systematic error for the charm jets are the uncertainty on the light jet contribution, the uncertainty of the impact parameter resolution and the contribution of the uncorrelated errors. For the beauty jets, the systematic uncertainties are considerably larger with the main sources of uncertainty being those due to the multiplicity of b quark decays, the track efficiency, the hadronic energy scale and the impact parameter resolution.

7   Results

The cross sections for c and b jets are presented in the laboratory frame of reference (section 7.1) and in the Breit frame (section 7.2). The b jet data are also compared with measurements obtained from muon tagging (section 7.3). The cross sections for events with c or b jets are shown together with theoretical predictions in table 2. The cross section values for all the measurements are given in table 3 with the contribution of the systematic errors for each measurement listed in table 4.

7.1 Jet Cross Sections in the Laboratory Frame

The jet cross sections in the laboratory frame are measured in the kinematic range $Q^2 > 6 \, \text{GeV}^2$ and $0.07 < y < 0.625$ for the heavy flavour jet with the highest E_T^{jet} with $E_T^{\text{jet}} > 6 \, \text{GeV}$ and $-1.0 < \eta^{\text{jet}} < 1.5$. The hadron level c and b cross sections with jets are

$$3290 \pm 50(\text{stat.}) \pm 260(\text{syst.}) \, \text{pb}$$

and

$$189 \pm 9(\text{stat.}) \pm 42(\text{syst.}) \, \text{pb},$$

respectively. Here the first error is statistical and the second is systematic.

These cross sections are compared in table 2 to the expectations of the Monte Carlo programs RAPGAP and CASCADE as well as to the NLO predictions with HVQDIS including hadronisation corrections. The NLO predictions are given for three different sets of PDFs and two different scale choices, $\mu = \sqrt{(Q^2 + p_T^2 + m^2)/2}$ and $\mu = \sqrt{Q^2 + 4m^2}$. Overall, RAPGAP agrees well with data for both charm and beauty. CASCADE predicts c and b cross sections which are around 20% higher than the data. Within uncertainties the NLO predictions agree reasonably well with the data both for charm and beauty. In general the NLO expectations for beauty display a smaller dependence on scale than for charm.

Differential c and b jet cross sections are measured as a function of E_T^{jet}, η^{jet}, Q^2, and the number of jets N^{jet} with $E_T^{\text{jet}} > 6 \, \text{GeV}$ (table 3). The differential c cross sections are shown in figure 3 in comparison to Monte Carlo expectations. Also included in the figure is a comparision of shape of each Monte Carlo distribution to that of the data (R^{norm}). These distributions are evaluted by taking the ratio of the Monte Carlo to data differential cross section and dividing by the Monte Carlo to data ratio of the total cross section integrated across the distribution.

As expected from the visible cross section given in table 2 the RAPGAP model describes the normalisation of the cross section distributions reasonably well, whereas CASCADE lies around 20% above the data on average. In the comparison of the shapes of the distributions both RAPGAP and CASCADE give a reasonable, although not perfect, description of the data. In general the data lies between the predictions of the two models, with the exception of the N^{jet} distribution, where RAPGAP is in better agreement with the data for $N^{\text{jet}} = 2$.

The charm jet cross section measurements are shown in figure 4 together with the NLO predictions of HVQDIS. In general the NLO expectations describe the data reasonably well in all differential distributions although the predictions with the scale $\mu = \sqrt{(Q^2 + p_T^2 + m^2)/2}$ fall somewhat below the data at low Q^2, low E_T^{jet} and in the forward η^{jet} region.

In figures 5 and 6 the differential b cross sections are shown as a function of E_T^{jet}, η^{jet}, Q^2 and N^{jet} in comparison to Monte Carlo and NLO expectations, respectively. RAPGAP yields a good description of all distributions for beauty. As with charm, the CASCADE model predictions lie around 20% above the data on average. The model is, however, able to provide a reasonable description of the shapes of the beauty jet cross sections. HVQDIS gives a good description of the beauty data with little dependence on the choice of scale.

13

7.2 Jet Cross Sections in the Breit Frame

Differential c and b cross sections are also measured for the highest E_T^{*jet} jet in the Breit frame with $E_T^{*jet} > 6$ GeV in the kinematic range $Q^2 > 6$ GeV^2, $0.07 < y < 0.625$ for the heavy flavour jet with the highest E_T^{jet} in the laboratory satisfying $E_T^{jet} > 1.5$ GeV and $-1.0 < \eta^{jet} < 1.5$.

The c cross sections are shown as a function of Q^2 and E_T^{*jet} in figure 7. The data are compared to the expectations from RAPGAP, CASCADE and HVQDIS. As in the laboratory frame the RAPGAP model provides a reasonable description of the charm data whereas CASCADE predicts a higher rate than the data, but here the difference is larger and is around 40%. In comparison with the shapes of the data both models provide a good description of the E_T^{*jet} cross section whilst neither model gives a perfect description of the Q^2 distribution. As for the laboratory frame analysis, HVQDIS with the scale choice $\mu = \sqrt{Q^2 + 4m^2}$ reproduces the data well, while for the scale $\mu = \sqrt{(Q^2 + p_T^2 + m^2)/2}$ it tends to underestimate the c jet data at low values of Q^2 and E_T^{*jet}.

The differential b cross sections are shown as a function of Q^2 and E_T^{*jet} in figure 8 together with the Monte Carlo and NLO expectations. As for charm, RAPGAP provides a reasonable description of the data whereas CASCADE lies around 40% higher. Both models provide a reasonable description of the shapes of the data in the Breit frame. The higher rate of Breit frame jets in CASCADE both for charm and beauty jet production is related to the transverse momentum distribution of the unintegrated gluon density used for the calculations. HVQDIS describes the data well showing little dependence on the choice of scales.

7.3 Comparison with Muon Tagging Measurements

The b jet cross sections may be compared with b jet measurements obtained from muon tagging in the Breit (H1 [7]) and laboratory (ZEUS [8]) frames of reference. The muon measurements were made requiring the presence of a muon and a jet in either the laboratory frame, with $E_T^{jet} > 5$ GeV or in the Breit frame with $E_T^{*jet} > 6$ GeV and with a central rapidity requirement in the laboratory frame, similar to the present analysis. The measurements were also made in a similar y range but start at lower values of Q^2 ($Q^2 > 2$ GeV^2). Therefore, comparison of the cross sections with these measurements as a function of E_T^{jet} or E_T^{*jet} would require interpolating over a large range in Q^2. However, the b cross sections can be compared as a function of Q^2 for the range where the Q^2 binning of the muon measurements overlaps closely with the present analysis, namely $Q^2 > 10$ GeV^2 for the laboratory analysis and $Q^2 > 6$ GeV^2 for the Breit frame analysis.

The present analysis is repeated with two different sets of Q^2 bins chosen to match the H1 and ZEUS muon measurements as closely as possible. The cross sections are shown as a function of Q^2 for the two sets of bins in figure 9. The H1 muon data are corrected by factors of about 15 which are obtained using the RAPGAP Monte Carlo. The dominant corrections account for the $b \rightarrow \mu$ branching fraction and for the extrapolation from the phase space of the muon measurement, which had restrictions on p_T^μ and η^μ, to the phase space of the present analysis. The ZEUS muon data are corrected to the present phase space by factors of around

6. These corrections are smaller than in the case of the H1 data because the ZEUS data have a wider η^μ and p_T^μ coverage. The corrections also include smaller effects due to the difference in the E_T range of the jets for the ZEUS laboratory frame analysis, differences in the η ranges of the jets, the difference in the y ranges, the difference in the jet cross section definitions and jet finding algorithms and the fact that the lower edge of the lowest Q^2 bin is $Q^2 \geq 5\ \mathrm{GeV}^2$ for the H1 muon measurement. An additional uncertainty of around 10% is added to the corrected muon measurements to account for theoretical uncertainties on the extrapolation factors coming from uncertainties on the perturbative scales and fragmentation model used. The central values of the present data in the Breit frame are found to lie below the adjusted H1 muon data at high Q^2. In the laboratory frame the present data are found to lie below the ZEUS muon data at low Q^2. In both cases the ratio of the muon data to the lifetime tagged data is around 2, although the measurements do agree when taking the full errors into account.

8   Conclusion

The cross sections for events with charm and beauty jets have been measured in deep inelastic scattering at the HERA electron–proton collider. Measurements are made in the laboratory frame for $E_T^{\mathrm{jet}} > 6\ \mathrm{GeV}$ and $-1.0 < \eta < 1.5$ for the kinematic region of photon virtuality $Q^2 > 6\ \mathrm{GeV}^2$ and inelasticity variable $0.07 < y < 0.625$. Measurements are also made in the Breit frame of reference. The analysis uses the precise spatial information from the H1 vertex detector to distinguish those jets that contain c and b flavoured hadrons from jets containing only light flavoured hadrons.

The laboratory frame jet data are compared with the Monte Carlo models RAPGAP and CASCADE. The RAPGAP model is generally found to give a reasonable description of the data. CASCADE is found to give predictions around 20% larger than the data but gives a reasonable description of the shapes of the differential cross section measurements. The data are also compared with NLO QCD calculations made using the HVQDIS program. The beauty data are well described by the calculation. The charm expectations are found to depend strongly on the choice of renormalisation and factorisation scale. The differential cross sections are described within the experimental and theoretical uncertainties with a scale choice of $\mu = \mu_r = \mu_f = \sqrt{Q^2 + 4m^2}$. The predictions tend to lie below the data at low Q^2 and high η with a choice of $\mu = \sqrt{(Q^2 + p_T^2 + m^2)/2}$.

For the measurements of the cross section requiring a jet in the Breit frame with $E_T^{*\mathrm{jet}} > 6\ \mathrm{GeV}$ RAPGAP is found to give a reasonable description of the data while CASCADE overestimates the cross sections, but gives also a reasonable description of the shapes of the differential cross section measurements. The NLO QCD predictions for charm jets with a scale choice of $\mu = \sqrt{Q^2 + 4m^2}$ are compatible with the data while the predictions with the choice of scale $\mu = \sqrt{(Q^2 + p_T^2 + m^2)/2}$ fail to describe the data at low Q^2. The b jet data are described by NLO QCD for all choices of scale.

The b jet data are compared with H1 and ZEUS data obtained from muon tagging by adjusting that data mainly for the extrapolation of the measured to the full muon phase space and for the $b \to \mu$ branching fraction. The central values of the b jet data from the present analysis are

15

found to lie below those obtained from ZEUS at low Q^2 and below the H1 muon tagged data at high Q^2, although the measurements agree within errors.

The present measurements show that charm and beauty production in deep inelastic scattering, adequately described by NLO QCD in the inclusive case, is also described in the presence of an additional hard scale provided by a jet.

Acknowledgements

References

[1] F. D. Aaron *et al.* [H1 Collaboration], Eur. Phys. J. C **65** (2010) 89 [arXiv:0907.2643];

A. Aktas *et al.* [H1 Collaboration], Eur. Phys. J. C **40** (2005) 349 [hep-ex/0411046].

[2] A. Aktas *et al.* [H1 Collaboration], Eur. Phys. J. C **45** (2006) 23 [hep-ex/0507081].

[3] C. Adloff *et al.* [H1 Collaboration], Z. Phys. C **72** (1996) 593 [hep-ex/9607012];

J. Breitweg *et al.* [ZEUS Collaboration], Phys. Lett. B **407** (1997) 402 [hep-ex/9706009];

C. Adloff *et al.* [H1 Collaboration], Nucl. Phys. B **545** (1999) 21 [hep-ex/9812023];

J. Breitweg *et al.* [ZEUS Collaboration], Eur. Phys. J. C **12** (2000) 35 [hep-ex/9908012];

S. Chekanov *et al.* [ZEUS Collaboration], Phys. Rev. D **69** (2004) 012004 [hep-ex/0308068];

S. Chekanov *et al.* [ZEUS Collaboration], Eur. Phys. J. C **63** (2009) 171 [arXiv:0812.3775].

[4] C. Adloff *et al.* [H1 Collaboration], Phys. Lett. B **528** (2002) 199 [hep-ex/0108039];

F. D. Aaron *et al.* [H1 Collaboration], Phys. Lett. B **686** (2010) 91 [arXiv:0911.3989].

[5] S. Chekanov *et al.* [ZEUS Collaboration], Eur. Phys. J. C **65** (2010) 65 [arXiv:0904.3487].

[6] S. Chekanov *et al.* [ZEUS Collaboration], Phys. Lett. B **599** (2004) 173 [hep-ex/0405069].

[7] A. Aktas *et al.* [H1 Collaboration], Eur. Phys. J. C **41** (2005) 453 [hep-ex/0502010].

[8] H. Abramowicz *et al.* [ZEUS Collaboration], arXiv:1005.3396.

[9] C. Adloff *et al.* [H1 Collaboration], Phys. Lett. B **467** (1999) 156 [Erratum-ibid. B **518** (2001) 331] [hep-ex/9909029];

J. Breitweg *et al.* [ZEUS Collaboration], Eur. Phys. J. C **18** (2001) 625 [arXiv:hep-ex/0011081];

A. Aktas *et al.* [H1 Collaboration], Phys. Lett. B **621** (2005) 56 [hep-ex/0503038];

S. Chekanov *et al.* [ZEUS Collaboration], Eur. Phys. J. C **50** (2007) 299 [hep-ex/0609050];

S. Chekanov *et al.* [ZEUS Collaboration], JHEP **0902** (2009) 032 [arXiv:0811.0894].

[10] S. Chekanov *et al.* [ZEUS Collaboration], Phys. Rev. D **70** (2004) 012008 [Erratum-ibid. D **74** (2006) 059906] [hep-ex/0312057];

S. Chekanov *et al.* [ZEUS Collaboration], JHEP **0904** (2009) 133 [arXiv:0901.2226];

S. Chekanov *et al.* [ZEUS Collaboration], Phys. Rev. D **78** (2008) 072001 [arXiv:0805.4390].

[11] A. Aktas *et al.* [H1 Collaboration], Eur. Phys. J. C **51** (2007) 271 [hep-ex/0701023].

[12] A. Aktas *et al.* [H1 Collaboration], Eur. Phys. J. C **47** (2006) 597 [hep-ex/0605016].

[13] B. W. Harris and J. Smith, Phys. Rev. D **57** (1998) 2806 [hep-ph/9706334];
B. W. Harris and J. Smith, Nucl. Phys. B **452** (1995) 109;
B. W. Harris and J. Smith, Phys. Lett. B **353** (1995) 535.

[14] RAPGAP 3.1, H. Jung, Comput. Phys. Commun. **86** (1995) 147
(see also http://www.desy.de/∼jung/rapgap/).

[15] G. Ingelman and G. A. Schuler, Z. Phys. C **40** (1988) 299;

G. A. Schuler, Nucl. Phys. B **299**, 21 (1988).

[16] A. D. Martin, W. J. Stirling and R. S. Thorne, Phys. Lett. B **636** (2006) 259 [hep-ph/0603143].

[17] B. Andersson, G. Gustafson, G. Ingelman and T. Sjöstrand, Phys. Rept. **97** (1983) 31.

[18] PYTHIA 6.2, T. Sjöstrand *et al.*, Comput. Phys. Commun. **135** (2001) 238;

T. Sjöstrand, L. Lönnblad and S. Mrenna, hep-ph/0108264.

[19] M. G. Bowler, Z. Phys. C **11** (1981) 169.

[20] S. Schael *et al.* [ALEPH Collaboration], Phys. Lett. B **606** (2005) 265; G. Rudolph [ALEPH Collaboration], private communication.

[21] A. Kwiatkowski, H. Spiesberger and H. J. Möhring, Comput. Phys. Commun. **69** (1992) 155.

[22] GEANT 3, R. Brun, R. Hagelberg, M. Hansroul and J. C. Lassalle, CERN-DD-78-2-REV.

[23] H. Jung and G. P. Salam, Eur. Phys. J. C **19** (2001) 351 [hep-ph/0012143].

[24] H. Jung, Proceedings of 12th International Workshop on Deep Inelastic Scattering (DIS 2004), Strbske Pleso, Slovakia (2004) 299, [hep-ph/0411287];

M. Ciafaloni, Nucl. Phys. B **296** (1988) 49;

S. Catani, F. Fiorani and G. Marchesini, Phys. Lett. B **234** (1990) 339;

S. Catani, F. Fiorani and G. Marchesini, Nucl. Phys. B **336** (1990) 18;

G. Marchesini, Nucl. Phys. B **445** (1995) 49 [hep-ph/9412327].

[25] E. Laenen, S. Riemersma, J. Smith and W. L. van Neerven, Nucl. Phys. B **392** (1993) 162;

E. Laenen, S. Riemersma, J. Smith and W. L. van Neerven, Nucl. Phys. B **392** (1993) 229.

[26] F. D. Aaron *et al.* [H1 Collaboration], Eur. Phys. J. C **65**(2010) 363 [arXiv:0904.3870];

F. D. Aaron *et al.* [H1 Collaboration], Eur. Phys. J. C **67**(2010) 1 [arXiv:0911.5678].

[27] M. A. G. Aivazis, F. I. Olness and W. K. Tung, Phys. Rev. D **50** (1994) 3085 [hep-ph/9312318].

[28] M. A. G. Aivazis, J. C. Collins, F. I. Olness and W. K. Tung, Phys. Rev. D **50** (1994) 3102 [hep-ph/9312319];

M. Krämer, F. I. Olness and D. E. Soper, Phys. Rev. D **62** (2000) 096007 [hep-ph/0003035].

[29] P. M. Nadolsky *et al.*, Phys. Rev. D **78** (2008) 013004 [arXiv:0802.0007].

[30] R. S. Thorne and R. G. Roberts, Phys. Rev. D **57** (1998) 6871 [hep-ph/9709442];

R. S. Thorne and R. G. Roberts, Phys. Lett. B **421** (1998) 303 [hep-ph/9711223].

[31] R. S. Thorne, Phys. Rev. D **73** (2006) 054019 [hep-ph/0601245].

[32] M. Buza, Y. Matiounine, J. Smith and W. L. van Neerven, Phys. Lett. B **411** (1997) 211 [hep-ph/9707263];

A. Chuvakin, J. Smith and W. L. van Neerven, Phys. Rev. D **61** (2000) 096004 [hep-ph/9910250];

A. Chuvakin, J. Smith and W. L. van Neerven, Phys. Rev. D **62** (2000) 036004 [hep-ph/0002011].

[33] S. Alekhin and S. Moch, Phys. Lett. B **672** (2009) 166 [arXiv:0811.1412].

[34] A. D. Martin, W. J. Stirling, R. S. Thorne and G. Watt, [arXiv:1007.2624].

[35] A. D. Martin, W. J. Stirling, R. S. Thorne and G. Watt, Eur. Phys. J. C **63** (2009) 189 [arXiv:0901.0002].

[36] H. L. Lai *et al.* [CTEQ Collaboration], Eur. Phys. J. C **12** (2000) 375 [hep-ph/9903282].

[37] R. S. Thorne and W. K. Tung, Contribution to "HERA and the LHC: 4th Workshop on the Implications of HERA for LHC Physics", Geneva, Switzerland, 26-30 May 2008, [arXiv:0809.0714].

[38] B. Andersson, G. Gustafson and B. Soderberg, Z. Phys. C **20** (1983) 317.

[39] I. Abt *et al.* [H1 Collaboration], Nucl. Instrum. Meth. A **386** (1997) 310;
I. Abt *et al.* [H1 Collaboration], Nucl. Instrum. Meth. A **386** (1997) 348.

[40] T. Nicholls *et al.* [H1 SPACAL Group], Nucl. Instrum. Meth. A **374** (1996) 149.

[41] D. Pitzl *et al.*, Nucl. Instrum. Meth. A **454** (2000) 334 [hep-ex/0002044];
B. List, Nucl. Instrum. Meth. A **501** (2001) 49.

[42] M. Peez, "Recherche de déviations au Modèle Standard dans les processus de grande énergie transverse sur le collisionneur électron-proton HERA", Ph.D. thesis. Université de Lyon (2003), DESY-THESIS-2003-023

(available at http://www-h1.desy.de/publications/thesis_list.html);

B. Portheault, "Première mésure des sections efficaces de courant chargé et neutre avec le faisceau de positrons polarisés HERA II et analyses QCD-électrofaibles", Ph.D. thesis. Université Paris XI (2005), LAL-05-05

(available at http://www-h1.desy.de/publications/thesis_list.html).

[43] U. Bassler and G. Bernardi, Nucl. Instrum. Meth. A **361** (1995) 197 [hep-ex/9412004].

[44] S. D. Ellis and D. E. Soper, Phys. Rev. D **48** (1993) 3160 [hep-ph/9305266];
S. Catani, Y. L. Dokshitzer, M. H. Seymour and B. R. Webber, Nucl. Phys. B **406** (1993) 187.

[45] W. M. Yao *et al.* [Particle Data Group], J. Phys. G **33** (2006) 1.

[46] L. Gladilin, hep-ex/9912064.

[47] A. Aktas *et al.* [H1 Collaboration], Eur. Phys. J. C **38** (2005) 447 [hep-ex/0408149].

[48] D. Coffman *et al.* [MARK-III Collaboration], Phys. Lett. B **263** (1991) 135.

[49] D. Abbaneo *et al.* [LEP/SLD Heavy Flavour Working Group], LEPHF 2001-01
(available from http://lepewwg.web.cern.ch/LEPEWWG/heavy/).

[50] F. D. Aaron *et al.* [H1 Collaboration], Eur. Phys. J. C **59** (2009) 1 [arXiv:0808.1003].

bin	Q^2 range (GeV^2)	$E_T^{(*)\mathrm{jet}}$ range (GeV)	η^{jet} range	N^{jet}	ρ_l	ρ_c	ρ_b	χ^2/n.d.f.	C_{lc}	C_{lb}	C_{bc}
1	$Q^2 > 6$	$E_T^{\mathrm{jet}} > 6$	$-1.0 < \eta^{\mathrm{jet}} < 1.5$	≥ 1	1.178 ± 0.004	1.040 ± 0.015	0.95 ± 0.05	$46.3/49$	-0.95	0.52	-0.66
2	$Q^2 > 6$	$6 < E_T^{\mathrm{jet}} < 10$	$-1.0 < \eta^{\mathrm{jet}} < 1.5$	≥ 1	1.203 ± 0.006	1.028 ± 0.020	0.93 ± 0.11	$54.8/46$	-0.95	0.61	-0.77
3		$10 < E_T^{\mathrm{jet}} < 16$			1.142 ± 0.009	1.078 ± 0.030	1.00 ± 0.06	$34.8/45$	-0.95	0.54	-0.67
4		$16 < E_T^{\mathrm{jet}} < 24$			1.060 ± 0.016	1.092 ± 0.066	0.87 ± 0.09	$41.0/40$	-0.95	0.51	-0.64
5		$24 < E_T^{\mathrm{jet}} < 36$			1.080 ± 0.030	0.713 ± 0.158	0.93 ± 0.20	$16.0/30$	-0.96	0.50	-0.62
6	$Q^2 > 6$	$E_T^{\mathrm{jet}} > 6$	$-1.0 < \eta^{\mathrm{jet}} < -0.5$	≥ 1	1.112 ± 0.012	0.883 ± 0.035	0.98 ± 0.21	$36.9/40$	-0.95	0.57	-0.71
7			$-0.5 < \eta^{\mathrm{jet}} < 0.0$		1.127 ± 0.009	0.985 ± 0.027	0.92 ± 0.09	$47.5/44$	-0.95	0.52	-0.66
8			$0.0 < \eta^{\mathrm{jet}} < 0.5$		1.199 ± 0.008	1.020 ± 0.029	1.05 ± 0.08	$46.5/45$	-0.94	0.51	-0.64
9			$0.5 < \eta^{\mathrm{jet}} < 1.0$		1.213 ± 0.009	1.172 ± 0.033	0.87 ± 0.08	$37.9/43$	-0.95	0.50	-0.64
10			$1.0 < \eta^{\mathrm{jet}} < 1.5$		1.188 ± 0.014	1.209 ± 0.060	0.81 ± 0.14	$39.8/41$	-0.97	0.60	-0.73
11	$6 < Q^2 < 18$	$E_T^{\mathrm{jet}} > 6$	$-1.0 < \eta^{\mathrm{jet}} < 1.5$	≥ 1	1.387 ± 0.011	1.174 ± 0.033	0.78 ± 0.09	$40.4/43$	-0.95	0.53	-0.67
12	$18 < Q^2 < 45$				1.153 ± 0.008	1.109 ± 0.027	1.00 ± 0.10	$44.2/43$	-0.95	0.54	-0.68
13	$45 < Q^2 < 110$				1.091 ± 0.007	0.986 ± 0.028	1.11 ± 0.10	$44.0/45$	-0.95	0.53	-0.67
14	$110 < Q^2 < 316$				1.177 ± 0.011	0.917 ± 0.039	1.06 ± 0.10	$41.2/42$	-0.95	0.53	-0.67
15	$316 < Q^2 < 1000$				1.084 ± 0.016	0.866 ± 0.065	0.86 ± 0.12	$39.0/39$	-0.95	0.50	-0.63
16	$Q^2 > 6$	$E_T^{\mathrm{jet}} > 6$	$-1.0 < \eta^{\mathrm{jet}} < 1.5$	$= 1$	1.208 ± 0.005	1.034 ± 0.016	0.98 ± 0.06	$47.4/49$	-0.95	0.53	-0.67
17				$= 2$	0.918 ± 0.013	1.074 ± 0.045	0.88 ± 0.07	$42.7/40$	-0.95	0.53	-0.67
18	$Q^2 > 6$	$6 < E_T^{*\mathrm{jet}} < 10$	$-1.0 < \eta^{\mathrm{jet}} < 1.5$	≥ 1	1.068 ± 0.009	1.111 ± 0.029	0.86 ± 0.08	$44.7/44$	-0.95	0.56	-0.72
19		$10 < E_T^{*\mathrm{jet}} < 16$			0.948 ± 0.016	0.987 ± 0.055	1.02 ± 0.07	$41.9/41$	-0.95	0.53	-0.67
20		$16 < E_T^{*\mathrm{jet}} < 24$			0.803 ± 0.033	0.973 ± 0.129	0.86 ± 0.13	$33.1/33$	-0.96	0.50	-0.64
21	$6 < Q^2 < 18$	$E_T^{*\mathrm{jet}} > 6$	$-1.0 < \eta^{\mathrm{jet}} < 1.5$	≥ 1	1.276 ± 0.016	1.248 ± 0.047	0.76 ± 0.10	$35.6/40$	-0.95	0.54	-0.69
22	$18 < Q^2 < 45$				0.999 ± 0.014	1.120 ± 0.045	0.98 ± 0.09	$29.7/40$	-0.95	0.54	-0.69
23	$45 < Q^2 < 110$				0.864 ± 0.014	0.949 ± 0.049	1.04 ± 0.11	$42.6/39$	-0.95	0.53	-0.68
24	$110 < Q^2 < 316$				0.927 ± 0.018	0.945 ± 0.068	0.95 ± 0.12	$38.5/37$	-0.95	0.52	-0.67
25	$316 < Q^2 < 1000$				0.865 ± 0.024	0.775 ± 0.102	0.74 ± 0.15	$16.2/31$	-0.95	0.48	-0.62
26	$6 < Q^2 < 18$	$E_T^{*\mathrm{jet}} > 6$	$-1.0 < \eta^{\mathrm{jet}} < 1.5$	≥ 1	1.272 ± 0.016	1.250 ± 0.047	0.77 ± 0.10	$36.5/40$	-0.95	0.54	-0.68
27	$18 < Q^2 < 100$				0.944 ± 0.010	1.055 ± 0.034	1.01 ± 0.07	$31.9/43$	-0.95	0.54	-0.69
28	$10 < Q^2 < 25$	$E_T^{*\mathrm{jet}} > 6$	$-1.0 < \eta^{\mathrm{jet}} < 1.5$	≥ 1	1.277 ± 0.010	1.127 ± 0.029	0.86 ± 0.09	$42.9/43$	-0.95	0.53	-0.67
29	$25 < Q^2 < 100$				1.109 ± 0.006	1.044 ± 0.022	1.06 ± 0.08	$45.9/46$	-0.95	0.53	-0.68
30	$100 < Q^2 < 1000$				1.131 ± 0.009	0.919 ± 0.031	0.96 ± 0.08	$37.7/44$	-0.95	0.51	-0.65

Table 1: The fit parameters ρ_l, ρ_c and ρ_b along with their errors, the χ^2 per degree of freedom and the correlation coefficients. The first row lists the results of the fit used to evaluate the integrated cross sections (bin 1). The remaining rows lists the fits used to evaluate the differential cross sections for jets in the laboratory frame (bins 2–17 and 28–30) and those requiring at least one jet in the Breit frame (bins 18–27).

			charm jet σ [pb]	beauty jet σ [pb]
H1 Data			$\mathbf{3290 \pm 50 \pm 260}$	$\mathbf{189 \pm 9 \pm 42}$
Model	μ	PDF		
RAPGAP	Q^2	MRST2004F3LO	3170	199
CASCADE	$\sqrt{Q^2 + p_T^2 + 4m^2}$	A0	3900	248
NLO HVQDIS	$\sqrt{(Q^2 + p_T^2 + m^2)/2}$	MSTW08FF3	2780^{+230}_{-230}	199^{+23}_{-22}
	$\sqrt{Q^2 + 4m^2}$		3020^{+600}_{-320}	197^{+28}_{-22}
	$\sqrt{(Q^2 + p_T^2 + m^2)/2}$	CTEQ6.6	2780^{+240}_{-240}	196^{+24}_{-21}
	$\sqrt{Q^2 + 4m^2}$		3000^{+600}_{-310}	194^{+27}_{-22}
	$\sqrt{(Q^2 + p_T^2 + m^2)/2}$	CTEQ5F3	2550^{+210}_{-230}	180^{+21}_{-19}
	$\sqrt{Q^2 + 4m^2}$		2800^{+550}_{-320}	180^{+24}_{-21}

Table 2: The cross sections for events with c and b jets for the kinematic range $Q^2 > 6$ GeV^2, $0.07 < y < 0.625$, $E_T^{\mathrm{jet}} > 6$ GeV and $-1.0 < \eta^{\mathrm{jet}} < 1.5$. The measured data cross sections are shown with their statistical and systematic uncertainties. The data are compared with the predictions from the Monte Carlos RAPGAP and CASCADE and with NLO QCD, calculated using HVQDIS. The NLO QCD predictions are shown for three sets of parton distribution functions and two choices of renormalisation and factorisation scales. The errors are obtained by changing the scales by factors of 0.5 and 2, by varying the quark masses and using a different model for the fragmentation of the quarks.

bin	Q^2 range (GeV^2)	$E_T^{(*)\mathrm{jet}}$ range (GeV)	η^{jet} range	N^{jet}	σ (pb)	δ_{stat} (%)	δ_{sys} (%)	C_{had}
$c\,1$	$Q^2 > 6$	$E_T^{\mathrm{jet}} > 6$	$-1.0 < \eta^{\mathrm{jet}} < 1.5$	≥ 1	3292.3	1.4	7.9	1.00
$b\,1$					188.8	4.8	22.3	1.05
$c\,2$	$Q^2 > 6$	$6 < E_T^{\mathrm{jet}} < 10$	$-1.0 < \eta^{\mathrm{jet}} < 1.5$	≥ 1	2386.5	2.0	7.8	0.99
$b\,2$					100.9	11.8	34.3	1.14
$c\,3$		$10 < E_T^{\mathrm{jet}} < 16$			727.4	2.8	7.9	1.02
$b\,3$					67.5	6.3	20.4	0.96
$c\,4$		$16 < E_T^{\mathrm{jet}} < 24$			148.0	6.1	9.9	1.06
$b\,4$					16.5	10.4	17.6	0.91
$c\,5$		$24 < E_T^{\mathrm{jet}} < 36$			21.5	22.1	20.7	1.06
$b\,5$					3.4	21.8	17.8	0.96
$c\,6$	$Q^2 > 6$	$E_T^{\mathrm{jet}} > 6$	$-1.0 < \eta^{\mathrm{jet}} < -0.5$	≥ 1	449.6	4.0	6.9	1.11
$b\,6$					17.6	21.8	27.0	1.45
$c\,7$			$-0.5 < \eta^{\mathrm{jet}} < 0.0$		710.6	2.7	7.6	1.05
$b\,7$					36.6	10.0	23.6	1.04
$c\,8$			$0.0 < \eta^{\mathrm{jet}} < 0.5$		801.2	2.8	8.1	1.01
$b\,8$					53.2	7.7	22.7	0.98
$c\,9$			$0.5 < \eta^{\mathrm{jet}} < 1.0$		856.0	2.9	7.9	0.95
$b\,9$					43.9	9.7	20.8	1.01
$c\,10$			$1.0 < \eta^{\mathrm{jet}} < 1.5$		504.0	4.9	9.3	0.84
$b\,10$					32.7	17.5	25.3	1.04
$c\,11$	$6 < Q^2 < 18$	$E_T^{\mathrm{jet}} > 6$	$-1.0 < \eta^{\mathrm{jet}} < 1.5$	≥ 1	934.0	2.8	7.3	1.00
$b\,11$					44.2	12.2	25.1	1.07
$c\,12$	$18 < Q^2 < 45$				924.0	2.4	7.6	1.00
$b\,12$					49.1	9.6	23.8	1.07
$c\,13$	$45 < Q^2 < 110$				857.3	2.8	8.2	1.00
$b\,13$					51.7	9.2	22.0	1.05
$c\,14$	$110 < Q^2 < 316$				471.7	4.3	9.2	0.99
$b\,14$					36.4	9.5	19.7	1.01
$c\,15$	$316 < Q^2 < 1000$				113.8	7.5	10.3	1.00
$b\,15$					9.5	14.3	18.0	1.00
$c\,16$	$Q^2 > 6$	$E_T^{\mathrm{jet}} > 6$	$-1.0 < \eta^{\mathrm{jet}} < 1.5$	$= 1$	2938.4	1.5	7.9	0.99
$b\,16$					153.2	5.9	24.3	1.02
$c\,17$				$= 2$	337.3	4.2	7.7	1.04
$b\,17$					36.3	8.2	17.2	1.15
$c\,18$	$Q^2 > 6$	$6 < E_T^{*\mathrm{jet}} < 10$	$-1.0 < \eta^{\mathrm{jet}} < 1.5$	≥ 1	1083.5	2.6	7.8	1.00
$b\,18$					71.3	8.8	27.2	1.18
$c\,19$		$10 < E_T^{*\mathrm{jet}} < 16$			231.6	5.6	9.1	1.03
$b\,19$					39.7	7.4	18.2	0.95
$c\,20$		$16 < E_T^{*\mathrm{jet}} < 24$			39.7	13.2	15.0	1.04
$b\,20$					7.3	15.2	17.4	0.92
$c\,21$	$6 < Q^2 < 18$	$E_T^{*\mathrm{jet}} > 6$	$-1.0 < \eta^{\mathrm{jet}} < 1.5$	≥ 1	650.4	3.8	7.9	1.01
$b\,21$					37.2	12.6	25.5	1.09
$c\,22$	$18 < Q^2 < 45$				372.1	4.0	8.0	1.00
$b\,22$					34.0	9.6	22.5	1.10
$c\,23$	$45 < Q^2 < 110$				207.9	5.2	8.4	1.01
$b\,23$					26.0	10.2	19.7	1.09
$c\,24$	$110 < Q^2 < 316$				121.1	7.1	9.4	1.02
$b\,24$					15.3	12.3	19.7	1.08
$c\,25$	$316 < Q^2 < 1000$				34.5	13.2	13.7	1.01
$b\,25$					4.3	20.0	17.9	1.07
$c\,26$	$6 < Q^2 < 18$	$E_T^{*\mathrm{jet}} > 6$	$-1.0 < \eta^{\mathrm{jet}} < 1.5$	≥ 1	657.7	3.7	7.9	1.01
$b\,26$					37.6	12.5	25.4	1.09
$c\,27$	$18 < Q^2 < 100$				557.6	3.2	8.0	1.01
$b\,27$					57.3	7.1	21.1	1.10
$c\,28$	$10 < Q^2 < 25$	$E_T^{*\mathrm{jet}} > 6$	$-1.0 < \eta^{\mathrm{jet}} < 1.5$	≥ 1	811.3	2.6	7.1	1.00
$b\,28$					41.6	10.7	23.9	1.07
$c\,29$	$25 < Q^2 < 100$				1400.1	2.1	8.0	1.00
$b\,29$					77.9	7.7	22.7	1.06
$c\,30$	$100 < Q^2 < 1000$				664.0	3.4	9.1	0.99
$b\,30$					47.5	7.9	19.8	1.01

Table 3: The measured charm and beauty cross sections for those events in which the highest E_T^{jet} jet is a charm or beauty jet. Integrated cross sections in each bin are shown. The first two rows (bin 1) are the integrated charm and beauty cross sections for the measured phase space respectively. The differential cross sections may be formed from the remaining rows by dividing by the corresponding bin width. The remaining rows list the cross sections for jets in the laboratory frame (bins 2–17 and 28–30) and those requiring at least one jet in the Breit frame (bins 18–27). The data is corrected to the hadron level. The table also shows the statistical (δ_{stat}) and systematic error (δ_{sys}), together with the hadronic correction C_{had} that is applied to the NLO theory to compare with the data.

bin	δ_{unc} (%)	δ_{res} (%)	δ_{treff} (%)	δ_{fragC} (%)	δ_{fragB} (%)	δ_{uds} (%)	$\delta_{\phi}^{\mathrm{jet}}$ (%)	δ_{hadE} (%)	δ_{gp} (%)	δ_{E_e} (%)	δ_{θ_e} (%)	$\delta_{P_T c}$ (%)	$\delta_{P_T b}$ (%)	$\delta_{\eta c}$ (%)	$\delta_{\eta b}$ (%)	$\delta_{\mathrm{BF}D+}$ (%)	$\delta_{\mathrm{BF}D0}$ (%)	$\delta_{\mathrm{Mult}D+}$ (%)	$\delta_{\mathrm{Mult}D0}$ (%)	$\delta_{\mathrm{Mult}D_s}$ (%)	$\delta_{\mathrm{Mult}B}$ (%)
c 1	2.0	2.0	0.7	−1.2	0.1	−4.5	1.8	1.4	0.6	0.2	0.6	0.3	0.9	1.0	−0.1	−0.3	0.1	−1.2	−1.2	−1.5	−1.3
b 1	2.0	−6.5	9.0	0.1	−2.1	2.0	0.9	7.2	0.8	−1.0	0.3	−4.1	−8.4	−0.3	2.1	−1.6	0.9	−4.4	−1.3	−1.9	13.1
c 2	2.0	2.4	0.6	−1.3	0.1	−4.5	1.4	1.6	0.8	0.3	0.7	0.7	0.2	1.2	−0.1	−0.1	0.0	−0.9	−1.2	−1.4	−0.7
b 2	2.0	−14.7	15.7	−1.8	−2.8	4.5	0.2	17.8	0.6	−1.2	0.2	−2.8	−3.7	0.9	4.1	−4.3	3.0	−10.8	−1.9	−3.7	11.8
c 3	2.0	2.3	0.3	−0.9	0.3	−4.2	2.2	−0.3	0.4	−0.1	0.4	1.2	0.3	1.2	−0.5	−0.2	0.1	−1.1	−1.1	−1.4	−2.3
b 3	2.0	−4.7	8.0	0.3	−2.3	1.4	0.8	8.4	0.7	−0.7	0.5	−0.7	−1.1	0.8	4.1	−1.1	0.4	−3.0	−1.3	−1.3	14.0
c 4	2.0	2.6	0.4	−0.6	0.2	−5.6	4.3	−0.6	0.1	−0.5	0.3	1.6	0.2	1.8	−0.6	−0.3	0.2	−1.1	−1.0	−1.3	−3.1
b 4	2.0	−2.9	7.0	0.1	−1.8	2.0	0.3	1.6	1.1	−0.5	0.3	−0.4	0.4	0.6	3.6	−0.5	0.0	−1.9	−1.1	−1.5	14.2
c 5	2.0	2.6	0.7	−1.1	0.4	−16.1	9.8	−1.0	−1.0	0.9	0.0	1.7	−0.1	2.1	−1.0	−0.3	0.1	−1.2	−1.3	−0.6	−5.3
b 5	2.0	0.6	7.5	0.3	−2.0	3.5	2.2	0.4	0.3	−2.1	0.1	−0.1	2.0	0.4	4.2	−0.1	−0.1	−0.8	−0.7	−1.6	13.8
c 6	2.0	2.3	0.4	−0.8	0.1	−3.3	1.2	1.2	0.3	−0.7	0.6	0.9	0.4	−1.0	0.0	−0.1	0.0	−1.0	−1.2	−1.5	−0.6
b 6	2.0	−10.0	14.2	−0.7	−1.2	1.6	2.1	11.0	1.1	−2.5	−0.3	−4.6	−4.8	−0.2	−3.1	−3.3	2.5	−8.8	−2.1	−2.9	10.6
c 7	2.0	2.0	0.7	−1.0	0.0	−4.4	1.5	1.4	0.7	−0.2	0.6	0.4	0.7	−0.2	0.0	−0.3	0.1	−1.2	−1.1	−1.4	−1.3
b 7	2.0	−6.9	10.6	0.6	−0.5	3.5	2.6	7.0	0.7	−1.1	0.4	−3.9	−6.9	−0.2	−1.1	−1.7	1.3	−4.8	−1.7	−2.8	14.2
c 8	2.0	2.2	0.8	−1.1	0.0	−4.5	2.3	1.2	0.4	−0.1	0.7	−0.2	1.0	0.2	0.0	−0.3	0.1	−1.2	−1.2	−1.5	−2.0
b 8	2.0	−6.0	8.2	0.3	−0.7	1.0	−0.5	5.5	0.9	−0.5	0.2	−3.1	−8.5	−0.1	−0.2	−1.2	0.7	−3.5	−1.1	−1.7	16.0
c 9	2.0	1.8	1.1	−1.0	0.0	−4.6	2.1	1.6	0.8	0.7	0.6	−0.4	0.9	0.7	0.0	−0.3	0.2	−1.3	−1.2	−1.4	−1.0
b 9	2.0	−4.2	9.0	0.4	−0.6	2.5	1.7	6.5	0.1	−0.9	0.4	−4.7	−9.6	0.0	1.0	−1.4	0.8	−4.2	−1.2	−1.4	11.0
c 10	2.0	2.3	0.4	−1.6	0.5	−6.2	1.5	0.6	0.7	2.4	0.6	0.8	1.4	1.9	0.0	−0.2	0.2	−1.0	−1.0	−1.3	−0.9
b 10	2.0	−7.6	10.6	−1.4	−5.8	3.2	5.0	9.1	1.2	−1.9	0.3	−7.5	−11.2	0.0	2.8	−1.8	1.1	−4.9	−1.7	−1.8	8.2
c 11	2.0	2.0	0.6	−1.3	0.1	−2.9	1.4	1.2	1.1	1.3	0.7	1.0	0.7	2.2	−0.1	−0.3	0.0	−1.1	−1.2	−1.4	−1.0
b 11	2.0	−7.6	11.7	0.3	−2.3	0.9	0.9	10.1	0.6	−0.5	0.5	−4.6	−7.8	0.0	4.0	−2.1	1.4	−6.2	−1.4	−2.4	12.5
c 12	2.0	2.1	0.7	−1.3	0.1	−3.8	1.6	2.1	0.8	0.7	0.2	0.9	0.7	0.9	−0.1	−0.2	0.1	−1.1	−1.3	−1.5	−1.0
b 12	2.0	−7.8	10.7	−0.2	−2.2	2.9	0.2	9.5	0.8	−0.7	0.2	−3.2	−7.1	−0.2	2.2	−2.1	1.3	−5.4	−1.3	−1.7	12.8
c 13	2.0	1.8	0.7	−1.1	0.2	−5.3	1.9	1.0	0.4	−0.2	0.7	0.0	0.7	0.3	−0.1	−0.2	0.1	−1.2	−1.3	−1.5	−1.6
b 13	2.0	−5.6	10.1	−0.1	−2.4	2.6	0.6	5.9	0.6	−1.2	0.4	−2.0	−6.4	0.3	1.4	−1.7	1.0	−4.5	−1.4	−2.2	14.2
c 14	2.0	2.2	0.6	−0.6	0.2	−5.9	2.6	0.5	0.1	−1.4	1.3	−1.0	0.8	1.1	−0.1	−0.3	0.2	−1.2	−1.0	−1.4	−2.5
b 14	2.0	−4.3	7.8	−0.1	−2.1	2.1	0.9	1.7	1.1	−0.4	0.0	−1.3	−6.1	0.1	2.7	−1.0	0.3	−3.0	−1.2	−1.2	14.6
c 15	2.0	2.6	0.7	−0.8	0.1	−7.1	3.3	0.1	0.0	−1.4	0.3	−0.4	0.5	1.1	−0.1	−0.4	0.2	−1.3	−0.9	−1.7	−2.8
b 15	2.0	−2.3	7.7	−0.1	−1.9	1.3	4.6	0.3	0.4	−1.6	0.7	−0.7	−3.3	0.4	1.9	−0.7	0.2	−2.0	−1.2	−1.1	13.6
c 16	2.0	2.0	0.8	−1.3	0.1	−4.7	1.7	1.5	0.6	0.3	0.6	0.4	0.9	1.0	−0.1	−0.3	0.1	−1.2	−1.2	−1.4	−1.3
b 16	2.0	−7.2	9.8	0.0	−2.6	2.5	0.8	8.7	0.7	−0.9	0.2	−4.5	−8.6	−0.2	2.3	−1.8	1.3	−5.1	−1.4	−2.2	14.0
c 17	2.0	2.6	−0.1	−0.6	0.1	−3.4	2.7	−0.1	0.8	−0.6	0.7	−0.2	1.0	1.5	−0.1	−0.2	0.1	−1.1	−1.0	−1.5	−2.1
b 17	2.0	−4.3	7.7	0.4	−0.7	0.7	1.2	4.3	1.7	−1.0	0.6	−2.0	−5.7	−0.2	2.0	−0.7	0.3	−2.4	−1.2	−0.9	11.2
c 18	2.0	2.4	0.3	−1.2	0.2	−3.6	2.3	0.5	1.7	0.8	0.9	−1.7	0.7	0.7	−0.2	−0.2	0.0	−1.0	−1.1	−1.3	−1.4
b 18	2.0	−7.3	10.1	0.5	−2.5	2.6	0.6	15.8	0.9	0.1	0.1	−3.5	−9.9	0.5	2.9	−1.8	1.0	−4.7	−1.5	−1.8	12.4
c 19	2.0	3.6	−0.4	−0.7	0.3	−3.8	3.2	−1.2	0.6	−1.7	0.8	−0.2	0.9	1.1	−0.7	−0.2	0.2	−1.0	−0.9	−1.2	−3.8
b 19	2.0	−3.4	6.0	0.2	−1.7	0.5	0.0	8.4	1.4	0.9	0.4	−0.9	−4.9	0.2	2.7	−0.5	−0.1	−1.4	−0.8	−0.9	12.3
c 20	2.0	7.0	−0.1	−1.6	0.3	−6.5	8.1	0.1	0.2	−2.5	0.1	1.3	0.8	2.4	−0.9	−0.2	0.2	−0.7	−0.9	−0.9	−5.1
b 20	2.0	−3.3	6.2	0.5	−1.9	1.7	−0.6	0.5	2.4	−0.1	0.6	−0.9	−2.2	0.1	3.6	−0.2	−0.2	−1.2	−0.9	−1.1	14.0
c 21	2.0	2.2	0.6	−1.0	0.1	−3.2	2.1	1.5	1.8	2.0	0.9	−1.4	0.8	1.9	−0.1	−0.3	0.0	−1.1	−1.1	−1.2	−1.3
b 21	2.0	−6.4	9.5	0.4	−2.1	1.6	0.7	13.4	0.8	−1.7	1.0	−3.5	−9.5	0.5	3.9	−1.5	0.9	−4.6	−1.5	−2.4	12.5
c 22	2.0	2.9	0.2	−1.3	0.2	−3.5	2.2	0.6	2.1	−0.1	1.0	−1.0	1.1	0.7	−0.3	−0.2	0.1	−1.0	−1.1	−1.3	−1.9
b 22	2.0	−5.5	7.9	0.6	−2.1	1.8	−0.1	11.1	0.9	2.1	−0.6	−2.4	−9.0	0.2	2.3	−1.2	0.5	−3.0	−1.2	−1.0	12.3
c 23	2.0	2.7	0.3	−1.0	0.3	−4.1	3.2	0.3	1.0	−1.2	0.8	−1.0	1.1	0.2	−0.4	−0.2	0.2	−1.1	−1.1	−1.2	−2.5
b 23	2.0	−4.2	7.4	0.3	−2.2	1.7	0.2	7.5	1.7	0.7	0.6	−1.6	−7.8	0.4	1.4	−0.7	0.3	−2.2	−0.9	−1.3	12.4
c 24	2.0	3.0	0.1	−0.7	0.2	−4.8	4.0	−0.3	0.2	−0.3	0.7	−1.6	0.9	1.0	−0.4	−0.2	0.2	−1.1	−0.9	−1.1	−3.3
b 24	2.0	−3.0	7.5	0.3	−2.1	1.9	0.1	4.9	3.1	0.0	0.2	−1.1	−7.5	0.5	3.1	−0.6	−0.1	−1.9	−1.2	−0.8	13.7
c 25	2.0	6.7	2.0	−1.3	0.2	−7.7	5.9	−2.1	−0.1	−1.1	−0.3	−1.3	0.6	0.8	−0.4	−0.3	0.2	−1.1	−1.0	−1.5	−3.1
b 25	2.0	−5.1	6.7	0.5	−1.9	1.4	4.2	2.6	1.1	−1.4	0.7	−0.8	−4.5	0.5	2.3	−0.4	−0.1	−1.7	−0.9	−1.3	12.8
c 26	2.0	2.2	0.5	−1.0	0.1	−3.2	2.0	1.5	1.8	1.9	1.1	−1.4	0.8	1.9	−0.1	−0.3	0.0	−1.1	−1.1	−1.2	−1.3
b 26	2.0	−6.4	9.6	0.4	−2.1	1.8	0.6	13.2	0.8	−1.3	0.4	−3.5	−9.5	0.5	3.9	−1.5	0.9	−4.5	−1.4	−2.3	12.6
c 27	2.0	2.6	0.2	−1.2	0.2	−3.8	2.8	0.5	1.7	−0.3	0.7	−1.1	1.1	0.5	−0.3	−0.2	0.1	−1.1	−1.1	−1.3	−2.1
b 27	2.0	−4.9	7.5	0.4	−2.1	1.7	−0.5	9.6	1.2	1.1	0.3	−2.0	−8.6	0.2	1.9	−1.0	0.4	−2.7	−1.1	−1.1	12.2
c 28	2.0	2.0	0.7	−1.4	0.1	−3.1	1.3	1.6	0.8	0.6	0.5	1.1	0.7	1.2	−0.1	−0.2	0.1	−1.1	−1.2	−1.4	−1.0
b 28	2.0	−6.9	10.6	0.3	−2.4	1.9	1.1	9.9	0.4	−0.6	0.3	−4.0	−7.3	0.2	2.7	−2.2	1.5	−5.9	−1.4	−2.2	12.5
c 29	2.0	1.9	0.7	−1.2	0.1	−4.8	1.9	1.6	0.7	0.3	0.4	0.3	0.7	0.7	−0.1	−0.2	0.1	−1.2	−1.3	−1.5	−1.2
b 29	2.0	−6.7	10.3	−0.3	−2.3	3.1	−0.9	7.6	0.8	−0.9	0.3	−2.5	−6.8	0.1	1.8	−1.9	1.1	−5.0	−1.3	−1.9	13.3
c 30	2.0	2.4	0.7	−0.7	0.1	−5.7	2.6	0.5	0.1	−1.4	1.0	−1.3	0.8	0.7	−0.1	−0.3	0.2	−1.2	−1.0	−1.5	−2.4
b 30	2.0	−5.0	7.5	0.0	−2.0	1.2	1.9	1.6	0.9	−0.9	0.2	−1.8	−7.0	0.2	2.0	−1.0	0.3	−2.8	−1.3	−1.3	14.4

Table 4: The contributions to the total systematic error. The bin numbering scheme follows that used in table 3. The first column lists the uncorrelated systematic error. The next 10 columns represent a $+1\sigma$ shift for the correlated systematic error contributions from: track impact parameter resolution; track efficiency; c fragmentation; b fragmentation; light quark contribution; struck quark angle ϕ_{quark}; hadronic energy scale; photoproduction background; electron energy scale; electron theta; reweighting the jet transverse momentum distribution P_T^{jet} and pseudorapidity η^{jet} distribution for c and b events; the c hadron branching fractions and multiplicities; and the b quark decay multiplicity. Only those uncertainties where there is an effect of $> 1\%$ in any bin are listed separately; the remaining uncertainties are included in the uncorrelated error. There is an additional contribution to the systematic error due to the uncertainty on the luminosity of 4%.
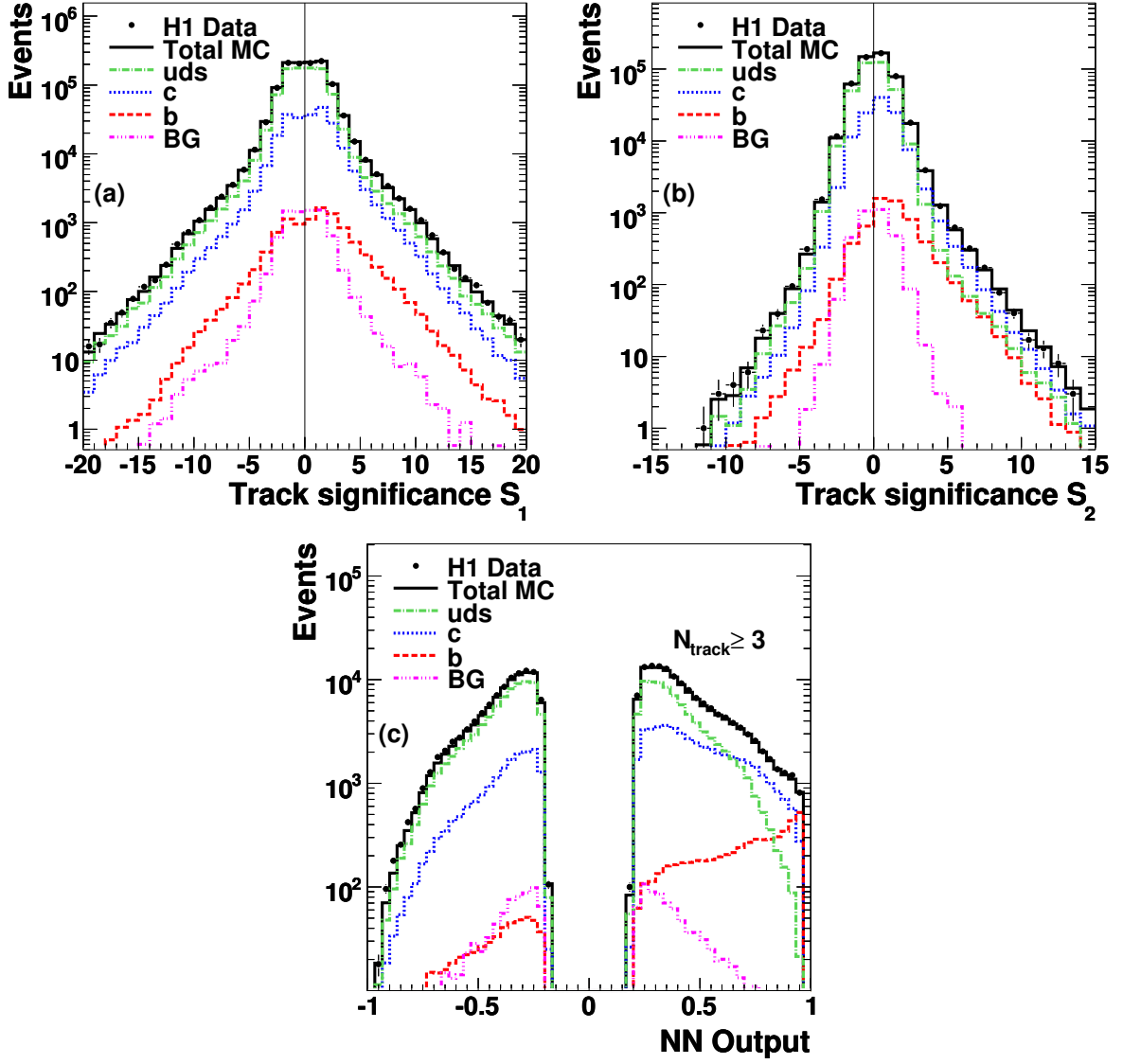
Figure 1: The significance distribution S_1 (a), S_2 (b) and the output of the neural network (NN Output) (c) for tracks of the highest transverse energy jet in the event. Included in the figure is the expectation from the Monte Carlo simulation for uds, c and b events. The contributions from the various quark flavours in the Monte Carlo simulation are shown after applying the scale factors ρ_l, ρ_c and ρ_b, as described in the text. The background (BG) contribution from a photoproduction Monte Carlo simulation is also shown.
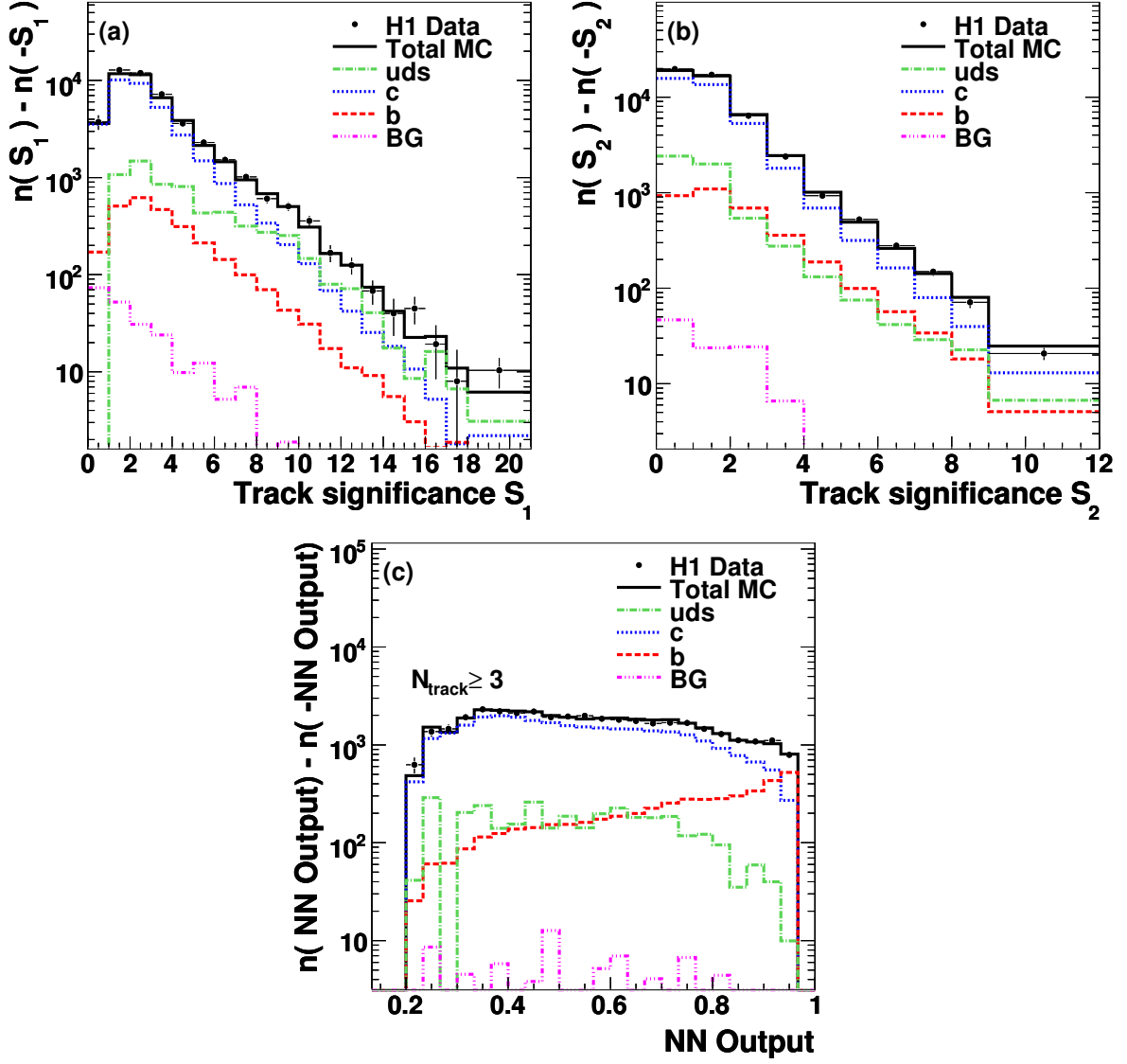
Figure 2: The subtracted distributions of S_1 (a), S_2 (b) and the neural network output (c) for the highest transverse energy jet in the event. Included in the figure is the result from the fit to the data of the Monte Carlo simulation distributions of the uds, c and b quark flavours to obtain the scale factors ρ_l, ρ_c and ρ_b, as described in the text. The background (BG) contribution from a photoproduction Monte Carlo simulation is also shown.
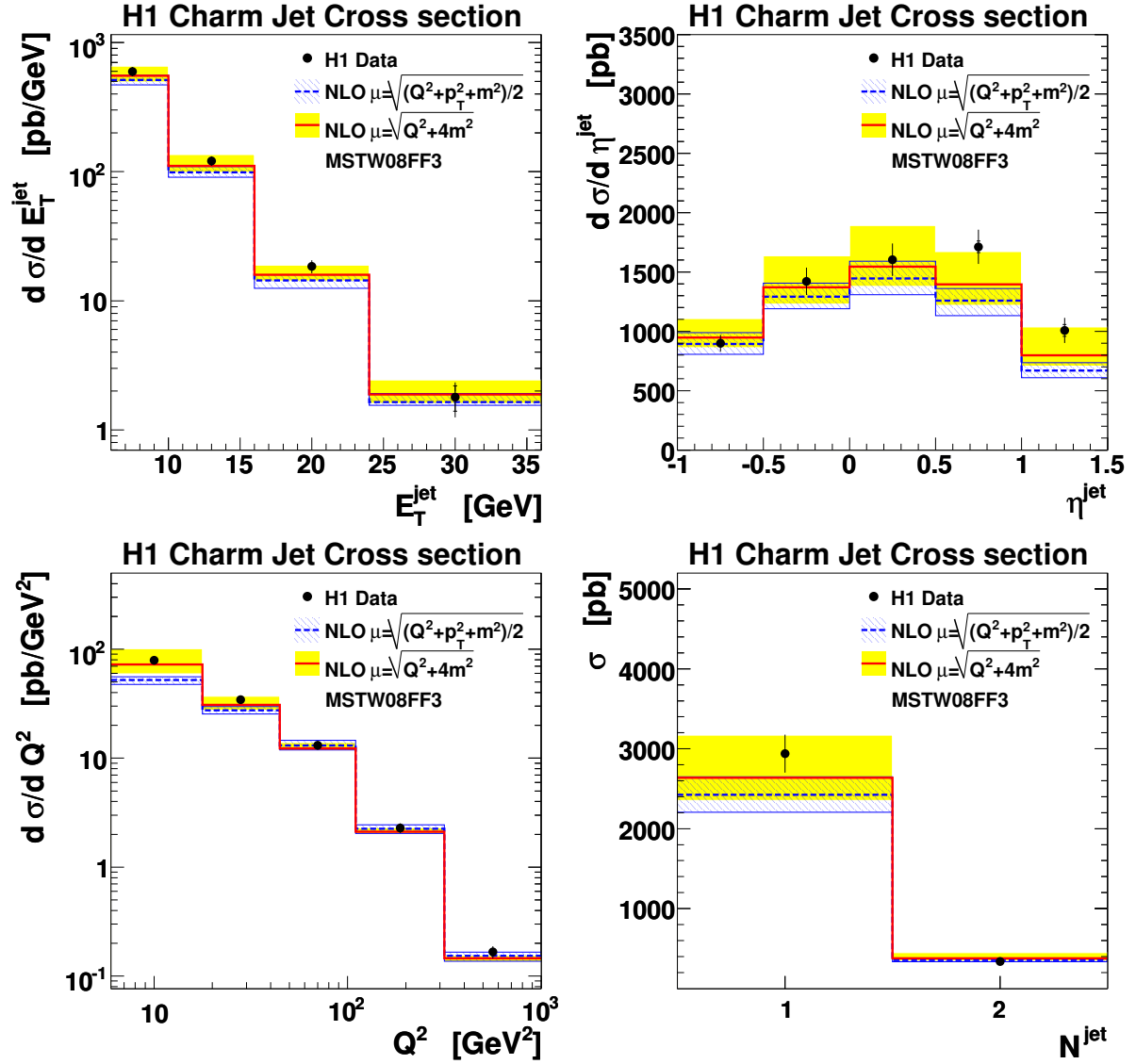
Figure 3: The differential cross sections for the highest transverse energy charm jet in the laboratory frame as a function of E_T^{jet}, η^{jet}, Q^2 and the number of laboratory frame jets in the event N^{jet}. The measurements are made for the kinematic range $E_T^{jet} > 6$ GeV, $-1 < \eta^{jet} < 1.5$, $Q^2 > 6$ GeV^2 and $0.07 < y < 0.625$. The inner error bars show the statistical error, the outer error bars represent the statistical and systematic errors added in quadrature. The data are compared with the predictions from the Monte Carlo models RAPGAP and CASCADE. The normalised theory to data ratio R^{norm} is also shown. The inner error bars on the data points at $R^{norm} = 1$ display the relative statistical errors, and the outer error bars show the relative statistical and systematic uncertainties added in quadrature.
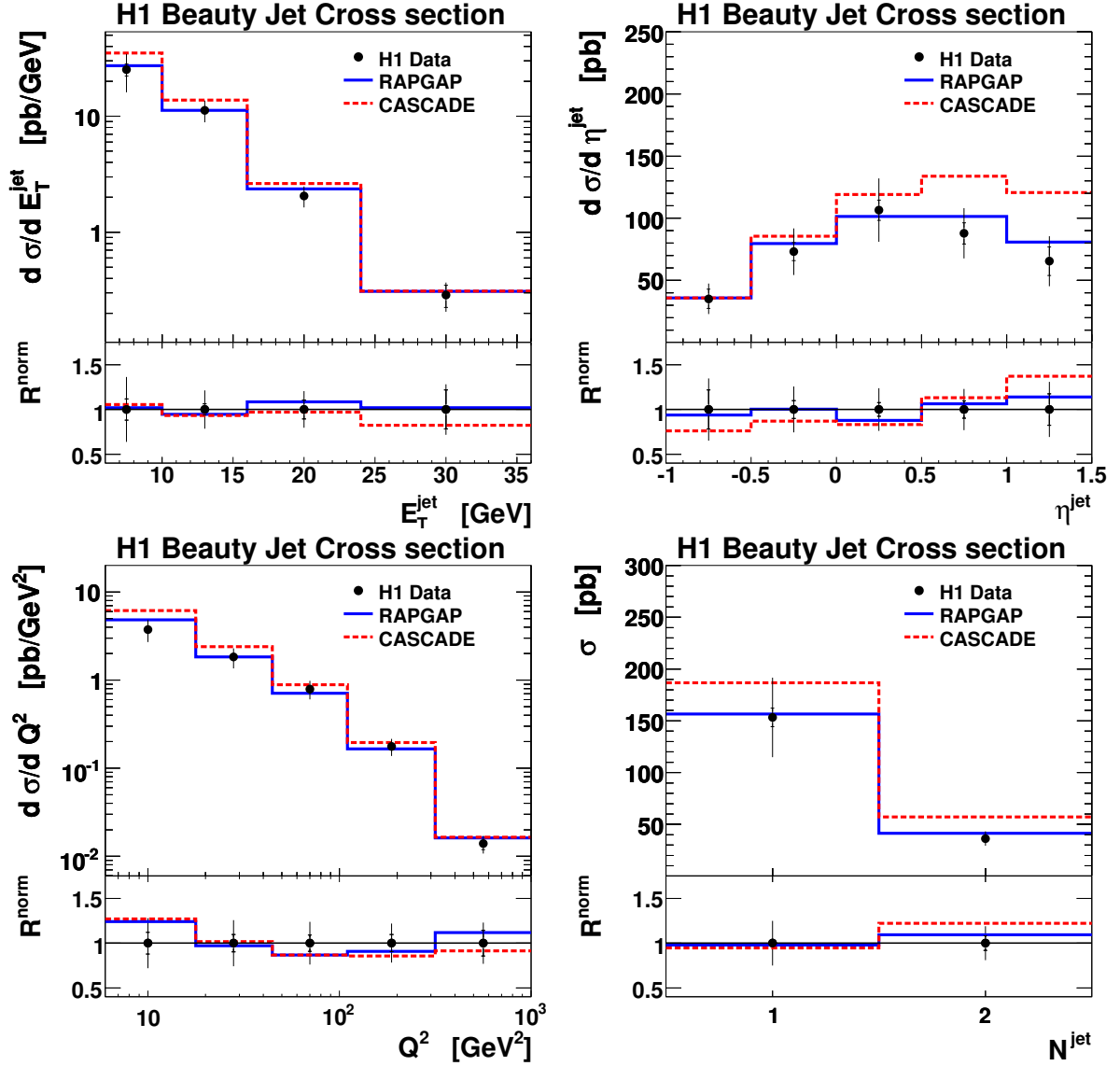
Figure 4: The differential cross sections for the highest transverse energy charm jet in the laboratory frame as a function of E_T^{jet}, η^{jet}, Q^2 and the number of laboratory frame jets in the event N^{jet}. The measurements are made for the kinematic range $E_T^{\text{jet}} > 6$ GeV, $-1 < \eta^{\text{jet}} < 1.5$, $Q^2 > 6$ GeV^2 and $0.07 < y < 0.625$. The inner error bars show the statistical error, the outer error bars represent the statistical and systematic errors added in quadrature. The data are compared with the predictions from NLO QCD where the bands indicate the theoretical uncertainties.

Figure 5: The differential cross sections for the highest transverse energy beauty jet in the laboratory frame as a function of E_T^{jet}, η^{jet}, Q^2 and the number of laboratory frame jets in the event N^{jet}. The measurements are made for the kinematic range $E_T^{\mathrm{jet}} > 6$ GeV, $-1 < \eta^{\mathrm{jet}} < 1.5$, $Q^2 > 6$ GeV^2 and $0.07 < y < 0.625$. The inner error bars show the statistical error, the outer error bars represent the statistical and systematic errors added in quadrature. The data are compared with the predictions from the Monte Carlo models RAPGAP and CASCADE. The normalised theory to data ratio R^{norm} is also shown. The inner error bars on the data points at $R^{\mathrm{norm}} = 1$ display the relative statistical errors, and the outer error bars show the relative statistical and systematic uncertainties added in quadrature.
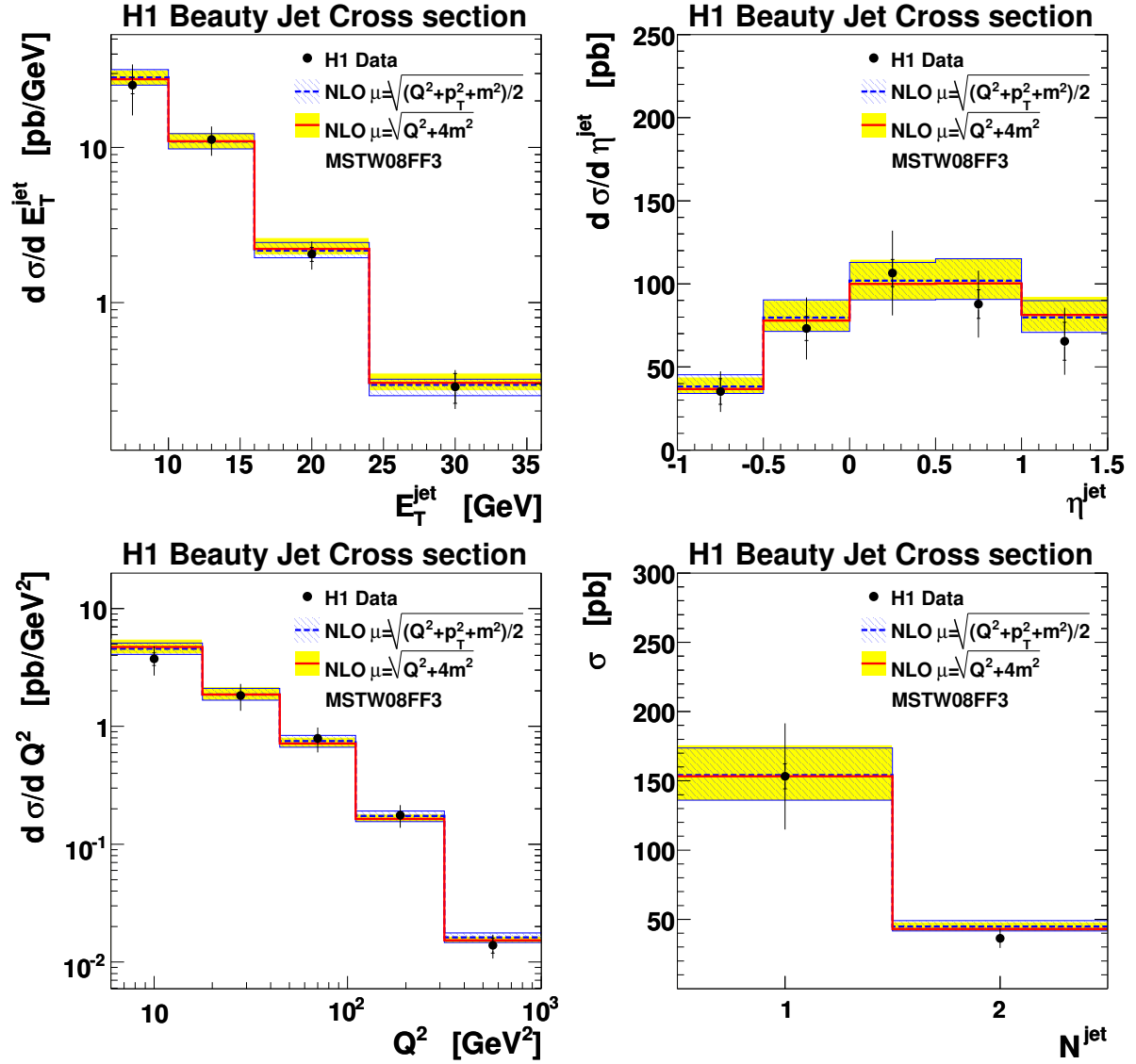
Figure 6: The differential cross sections for the highest transverse energy beauty jet in the laboratory frame as a function of E_T^{jet}, η^{jet}, Q^2 and the number of laboratory frame jets in the event N^{jet}. The measurements are made for the kinematic range $E_T^{\text{jet}} > 6$ GeV, $-1 < \eta^{\text{jet}} < 1.5$, $Q^2 > 6$ GeV^2 and $0.07 < y < 0.625$. The inner error bars show the statistical error, the outer error bars represent the statistical and systematic errors added in quadrature. The data are compared with the predictions from NLO QCD where the bands indicate the theoretical uncertainties.
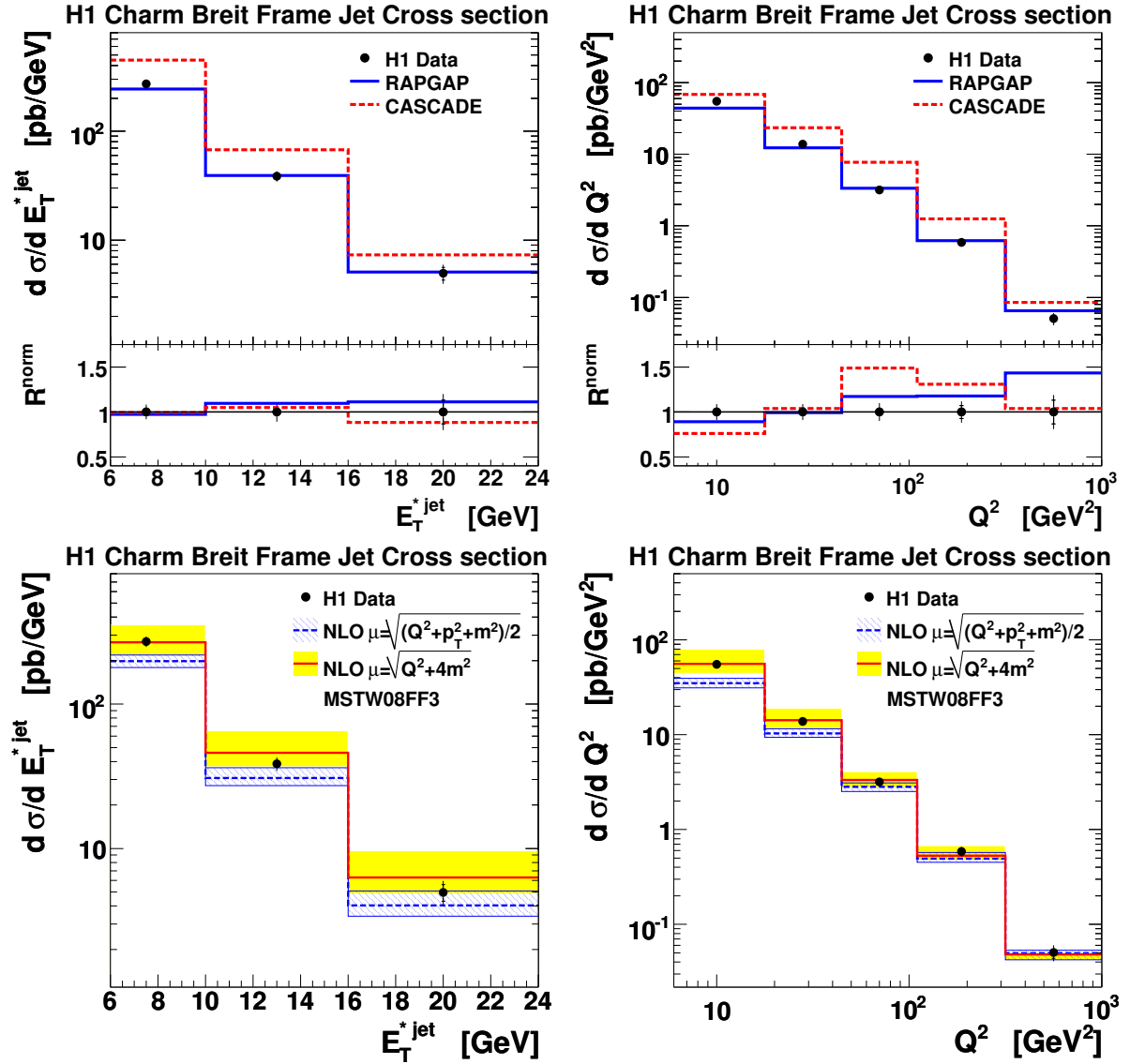
Figure 7: The differential cross sections $\mathrm{d}\sigma/\mathrm{d}E_T^{*\mathrm{jet}}$ and $\mathrm{d}\sigma/\mathrm{d}Q^2$ for events with a jet in the Breit frame, where the jet with the highest transverse energy in the laboratory frame satisfying $E_T^{\mathrm{jet}} > 1.5$ GeV and $-1 < \eta^{\mathrm{jet}} < 1.5$ is a charm jet. The measurements are made for the kinematic range $Q^2 > 6$ GeV^2 and $0.07 < y < 0.625$. The inner error bars show the statistical error, the outer error bars represent the statistical and systematic errors added in quadrature. The data are compared with the predictions from the Monte Carlo models RAPGAP and CASCADE (upper plots) and the NLO QCD calculation (lower plots), where the bands indicate the theoretical uncertainties. For the upper plots the normalised theory to data ratio R^{norm} is also shown. The inner error bars on the data points at $R^{\mathrm{norm}} = 1$ display the relative statistical errors, and the outer error bars show the relative statistical and systematic uncertainties added in quadrature.
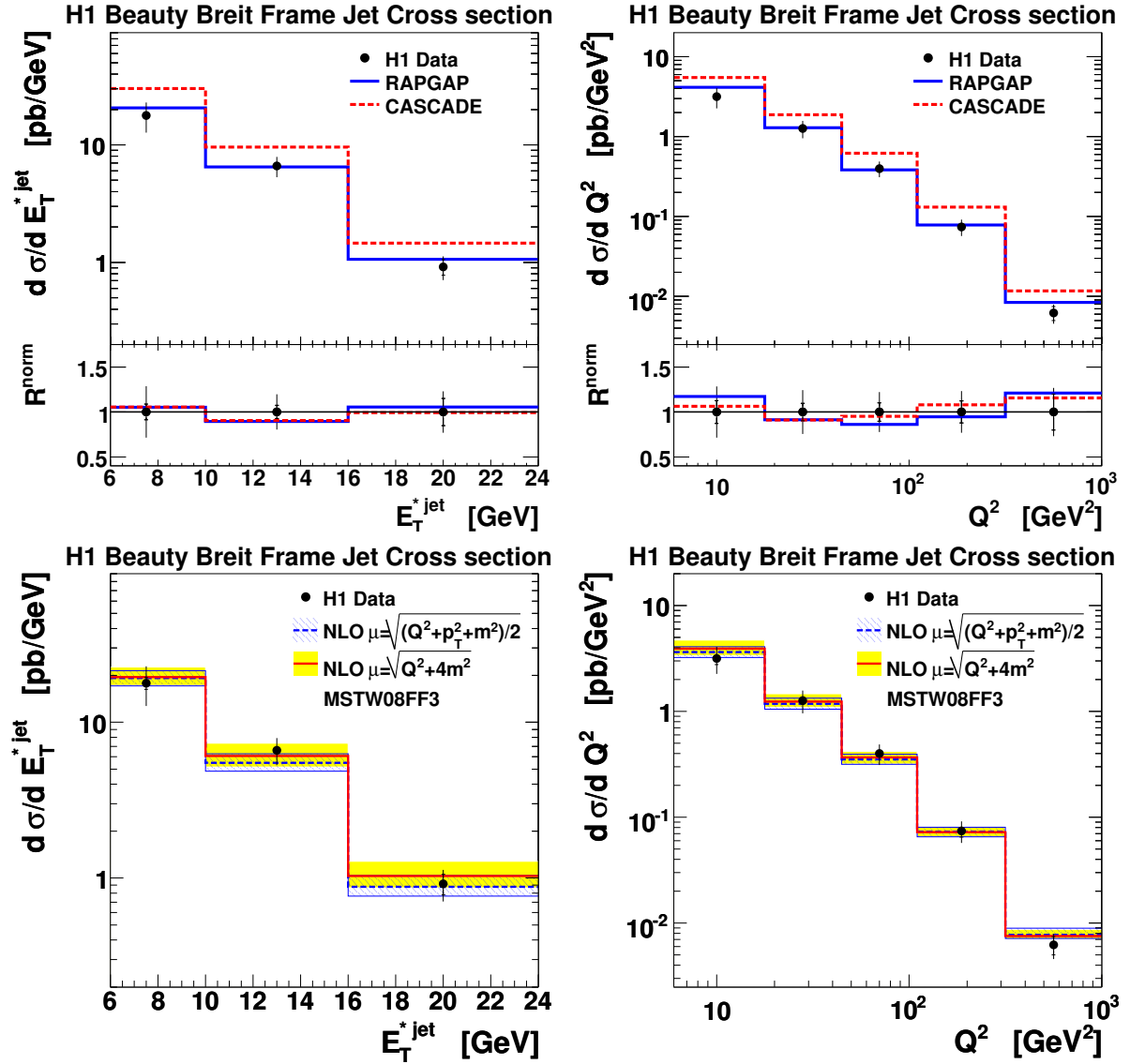
Figure 8: The differential cross sections $\mathrm{d}\sigma/\mathrm{d}E_T^{*\mathrm{jet}}$ and $\mathrm{d}\sigma/\mathrm{d}Q^2$ for events with a jet in the Breit frame, where the jet with the highest transverse energy in the laboratory frame satisfying $E_T^{\mathrm{jet}} > 1.5$ GeV and $-1 < \eta^{\mathrm{jet}} < 1.5$ is a beauty jet. The measurements are made for the kinematic range $Q^2 > 6$ GeV^2 and $0.07 < y < 0.625$. The inner error bars show the statistical error, the outer error bars represent the statistical and systematic errors added in quadrature. The data are compared with the predictions from the Monte Carlo models RAPGAP and CASCADE (upper plots) and the NLO QCD calculation (lower plots), where the bands indicate the theoretical uncertainties. For the upper plots the normalised theory to data ratio R^{norm} is also shown. The inner error bars on the data points at $R^{\mathrm{norm}} = 1$ display the relative statistical errors, and the outer error bars show the relative statistical and systematic uncertainties added in quadrature.
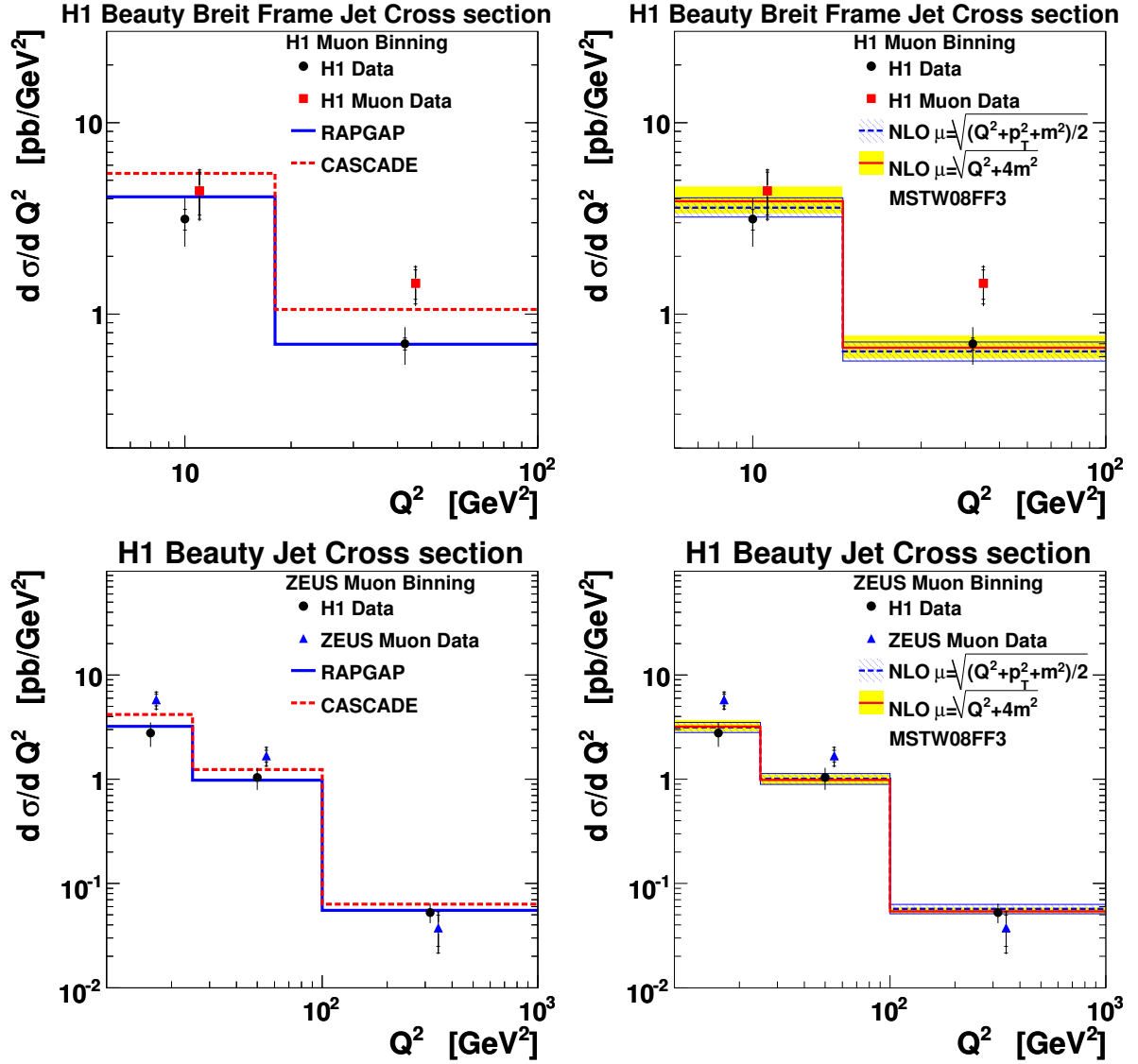
Figure 9: The upper plots show the differential cross section $\mathrm{d}\sigma/\mathrm{d}Q^2$ for events with a jet in the Breit frame with $E_T^{*\text{jet}} > 6\,\text{GeV}$, where the jet with the highest transverse energy in the laboratory frame satisfying $E_T^{\text{jet}} > 1.5\,\text{GeV}$ and $-1 < \eta^{\text{jet}} < 1.5$ is a beauty jet. The lower plots show the differential cross section $\mathrm{d}\sigma/\mathrm{d}Q^2$ for events with a beauty jet in the laboratory frame with $E_T^{\text{jet}} > 6\,\text{GeV}$ and $-1 < \eta^{\text{jet}} < 1.5$. The present measurements are made for the kinematic range $Q^2 > 6\,\text{GeV}^2$ and $0.07 < y < 0.625$. The inner error bars show the statistical error, the outer error bars represent the statistical and systematic errors added in quadrature. The data are compared with the measurements obtained using muon tagging from H1 [7] (upper plots) and ZEUS [8] (lower plots) extrapolated to the present phase space and shifted in Q^2 for visual clarity. For the muon data the outer error bars show the statistical, systematic and extrapolation uncertainties added in quadrature. The data are also compared with the predictions from the Monte Carlo models RAPGAP and CASCADE (left) and the NLO QCD calculation (right), where the bands indicate the theoretical uncertainties.